PHILOSOPHICAL TRANSACTIONS OF THE ROYAL SOCIETY A
MATHEMATICAL, PHYSICAL & ENGINEERING SCIENCES

On the Periodic Motion of a Circular Cylinder through a Linearly Stratified Fluid

Peter A. Davies, Don L. Boyer, Harindra J. S. Fernando and Xiuzhang Zhang

Phil. Trans. R. Soc. Lond. A 1994 **346**, 353-386
doi: 10.1098/rsta.1994.0025

On the periodic motion of a circular cylinder through a linearly stratified fluid†

By Peter A. Davies[1], Don L. Boyer[2],
Harindra J. S. Fernando[2] and Xiuzhang Zhang[2]

[1] *Department of Civil Engineering, The University, Dundee DD1 4HN, U.K.*
[2] *Department of Mechanical and Aerospace Engineering,*
The Arizona State University, Tempe, AZ 85287, U.S.A.

Contents

The results of a series of experiments on the periodic motion of a horizontal circular cylinder through a linearly stratified fluid are described. For cases in which the motion is composed of a uniform horizontal translation and a superimposed sinusoidal variation in horizontal velocity, a number of different flow types are identified, and régime diagrams delineating the boundaries between the flow types are presented. Conditions for forward overshooting of wake fluid are discussed, and suitable scaling criteria are derived for the occurrence of the overshooting phenomenon. Comparisons are made between the unsteady flow data and those pertaining to steady flow counterparts having the same instantaneous parameter values, and the conditions for the generation of flow phenomena associated solely with the periodic nature of the motion are discussed. Quantitative data are presented on the dependence of typical wake region dimensions on the controlling dimensionless parameters.

---

† This paper was produced from the authors' disk by using the TEX typesetting system.

Phil. Trans. R. Soc. Lond. A (1994) **345**, 353–386

Printed in Great Britain

1. Introduction

In a recent paper (Boyer *et al.* 1989 *a*), results were presented from a comprehensive investigation into the flow generated by a horizontal cylinder moving steadily through a stably stratified fluid. A number of previously unreported flow phenomena were described for this case, and it was confirmed that the character of the flow was determined principally by the individual values of the Reynolds and internal Froude numbers of the flow. Qualitative agreement between some of the experimental data and the predictions of a numerical model of Belotserkovskii *et al.* (1987) was demonstrated, and quantitative measurements of characteristic dimensions associated with (i) upstream blocking and (ii) turbulent downstream wakes were shown to accord well with scaling predictions. For one of the characteristic wake flows (*isolated vortices*), the experimental measurements have been shown subsequently (Davies *et al.* 1992) to be in consonance with measurements (Castro *et al.* 1990) of wave drag forces on cylinders moving steadily through stably stratified fluids.

The experiments of Boyer *et al.* (1989 *a*) have now been extended to include effects of unsteadiness in the motion of the cylinder, and data from these new experiments are presented here. A summary of some preliminary findings of the present investigation has been included in a review by Davies *et al.* (1992).

Thus far, studies of the effects of unsteadiness in the flow of a fluid past a circular cylinder have been dominated by cases involving homogeneous fluids, primarily because of the relevance of these cases to wave- and current-induced loadings on flexible offshore structures. Examples of such studies are those concerning the oscillating flow of a homogeneous fluid past a vertical cylinder, as considered by, for example, Keulegan & Carpenter (1958), Tanida *et al.* (1973), Griffin & Ramberg (1976), Bearman & Graham (1980), Bearman *et al.* (1981), Williamson (1985), Barti *et al.* (1986), Ongoren & Rockwell (1988 *a*, *b*), Obasaju *et al.* (1988), Sumer & Fredsøe (1988, 1989), Sumer *et al.* (1989), Bearman & Obasaju (1989), Garrison (1990) and Sumer *et al.* (1991). In the related context of sea bottom processes, studies on the oscillatory flow of homogeneous fluids over rippled beds have been reported recently by Blondeaux & Vittori (1991).

The only previous experiments of the type to be described here were the classical theoretical and experimental studies by Stevenson & Thomas (1969) and Stevenson (1973) on the phase configurations of internal waves generated by the travelling oscillatory motion of a cylinder in a stratified fluid. Though the results of these theoretical and experimental investigations are relevant to the present study (see below), the parameter ranges differed significantly from those of the present investigation. In particular, the earlier studies were concerned principally with linear, short-wavelength wave motions in relatively low Reynolds number flows, with small-amplitude forcing. Effects of flow separation at the body surface were not addressed specifically.

Other studies pertinent to the present investigation are those of (i) Bannon (1985), who studied oscillatory flow of a rotating, homogeneous fluid past a truncated upright vertical cylinder, and (ii) Boyer *et al.* (1989) and Boyer & Zhang (1990), who investigated the unsteady flow of a stratified, rotating fluid past an upright truncated obstacle. Finally in this regard, Sturova and her colleagues (unpublished work, 1986, 1989; Bukreev *et al.* 1986) have made several numerical studies of lee wave generation by the unsteady flow of a stratified fluid past a horizontal cylinder.

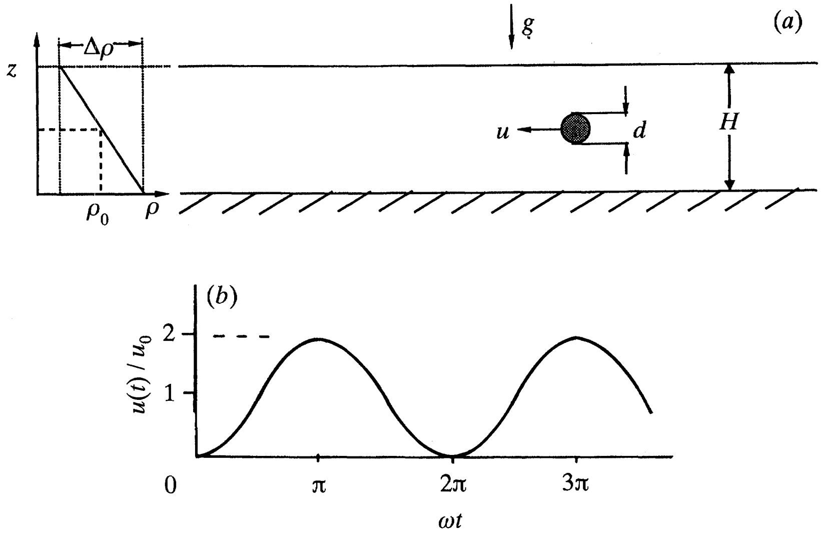

Figure 1. Schematic representation of (*a*) the experimental arrangement, and (*b*) the imposed velocity $u(t)$ of the horizontal cylinder.

2. Statement of the problem

The problem under consideration is the following (see figure 1 *a*): a horizontal circular cylinder of diameter d is immersed in a fluid of kinematic viscosity v and depth H. The fluid is stably stratified with an undisturbed linear density gradient,

$$\rho(z) = \rho_0 + (\tfrac{1}{2}\Delta\rho)(1 - 2z/H), \tag{2.1}$$

where ρ_0 is the density of the fluid at mid-depth and $\Delta\rho$ is the density difference between the bottom ($z = 0$) and the top ($z = H$) of the fluid. A horizontal cylinder, located at mid-depth ($z = \frac{1}{2}H$), is moved horizontally through the initially undisturbed fluid with a time-dependent velocity $u(t)$ given by

$$u(t) = u_0 - u_1 \cos \omega t, \tag{2.2}$$

with ω being the frequency of the oscillatory component of the motion (see figure 1 *b*). The resulting flow can then be described in terms of the following dimensionless parameters:

$Re = u_0 d/v,$	the Reynolds number,	(2.3)
$Fr = u_0/Nd,$	the internal Froude number,	(2.4)
$\Phi = u_1/u_0,$	the velocity ratio,	(2.5)
$\theta = \omega/N,$	the frequency ratio,	(2.6)

together with the geometrical ratios d/H, d/W and d/L. Here, W and L are the width and length respectively of the (rectangular) fluid container, and N is the buoyancy frequency (defined in the usual way as $N^2 = g\Delta\rho/\rho_0 H$, where g is the gravitational acceleration). Derived parameters of relevance to some of the ensuing discussion are (i) the Keulegan–Carpenter number $K = u_1/\omega d$, the ratio of the amplitude of the oscillation to the cylinder diameter, and (ii) the associated counterpart quantity $K_0 = u_0/\omega d$, based upon the mean velocity u_0. For cases in which $u_0 = u_1$ (as in the present experiments), $K = K_0$, but, in general, a distinction must be maintained between the two quantities. (The significance of the parameter K for free surface flows has been reviewed recently by Hudspeth (1991).)

3. The experimental apparatus

The experiments were carried out using long, stratified flow channels of the type described previously in Boyer *et al.* (1989*a*). Channels of length 9 m and 15 m respectively were used, and, in each case, the working section was filled slowly to a depth of 18 cm with a linearly stratified fluid, using the double reservoir technique described by Oster (1965). Common salt was used as the stratifying agent. Measurements of the undisturbed vertical density gradient in the tank were taken before the start of each run by withdrawing small samples of fluid at depth intervals of 1 cm, and measuring the density of each with a calibrated refractometer. The initially imposed density gradient was eroded with time by (i) the disturbance fields generated by the moving obstacle, (ii) surface evaporation, and (iii) the presence of an impermeable bottom surface. However, the erosion processes were typically very slow, and it was possible to perform six or seven experimental runs at 2–3 h intervals before the tank had to be re-filled and the density gradient re-established. In the experiments to be described, two values ($0.85\ \mathrm{s}^{-1}$; $1.15\ \mathrm{s}^{-1}$) of the buoyancy frequency were used. The following list summarizes the full ranges of the parameters investigated:

$$d = 1.6\ \mathrm{cm}; \quad H = 18.0\ \mathrm{cm}; \quad v = 0.01\ \mathrm{cm}^2\,\mathrm{s}^{-1};$$

$$\varPhi = u_1/u_0 = 1.0; \quad 0.85 \leqslant N \leqslant 1.15\ \mathrm{s}^{-1};$$

$$0.5 \leqslant u_0 \leqslant 3.0\ \mathrm{cm\,s}^{-1}; \quad 76 \leqslant Re \leqslant 648; \quad 0.20 \leqslant Fr \leqslant 3.70;$$

$$0.29 \leqslant \varTheta(=\omega/N) \leqslant 6.91; \quad 0.11 \leqslant K; \quad K_0 \leqslant 5.03.$$

The cylindrical obstacle was suspended at mid-depth in the fluid from an overhead carriage support. The ends of the cylinder were connected to the carriage by thin, rigid, slotted struts, the positions of which could be adjusted to ensure that the axis of the cylinder was horizontal. Small gaps (typically 1–2 mm) were left between the struts and the side walls of the tank to facilitate unhindered movement of the obstacle. The towing carriage, which also supported the experimental accessories required for flow visualization, was translated along the tank using a computer-controlled drive system. The form of the motion of the carriage (and thus the cylinder) was preset by entering the required values of u_0, u_1, and ω in the control software, and observations of the flow were made when the cylinder had reached a measurement section about halfway along the tank. (For all of the experiments reported here, the velocity ratio $\varPhi$ was always unity, so the cylinder came to rest instantaneously at the $\omega t = 2n\pi$ $(n = 0, 1, 2\ldots)$ positions in the forcing cycle).

A shadowgraph was used to visualize the flow structure, and a camera mounted on the carriage recorded the flow. Photographs were taken at pre-determined phase intervals within the oscillation cycle of the obstacle, the operation of the camera shutter being synchronized with the carriage motion and controlled by the drive software. For most of the runs, eight photographs per cycle were taken (i.e. at intervals of $\frac{1}{4}\pi$), though for cases in which the period of oscillation was comparable with the wind-on time of the camera motor drive, the number of photographs per cycle was reduced to four. For details of the shadowgraph arrangement, and the interpretation of the shadowgraph images, the reader is referred to the paper of Boyer *et al.* (1989 *a*). Finally, it is noted that some flow sequences were recorded photographically with the camera decoupled from the drive mechanism, and mounted at rest in the laboratory frame. With this arrangement, a sequence of shadowgraph images could be recorded at a fixed reference station as the cylinder passed, and the downstream wake could then be reconstructed from the image sequence. For some cases, the fixed camera was replaced at the reference station by a video camera; the wake pattern was then determined by matching and joining images of flow features in adjacent frames of the video record.

4. Results: flow classification

(*a*) *General features*

(*i*) *Hysteresis effects*

From the complete data-set of 115 experiments, the flow patterns were classified into thirteen characteristic flow types. Figures 2–13 show exemplary time sequences of twelve of these flow types, as observed with the obstacle moving with the periodic velocity represented in equation (2.2). In each sequence, except that shown in figure 2 (see later), five instantaneous shadowgraph images are presented for the following values of ωt: $2n\pi$, $2n\pi + (\frac{1}{2}\pi)$, $2n\pi + \pi$, $2n\pi + (\frac{3}{2}\pi)$, and $2(n+1)\pi$, $(n = 0, 1, 2 \ldots)$, respectively, so the third frame corresponds to the stage in the cycle where the obstacle velocity has its maximum value (see figure 1 *b*). In all cases, the first and last frames in each of these sequences show the flow with the cylinder instantaneously at rest in successive cycles.

The clearest common feature of all of the cases shown is the lack of any memory effects in the near wake flows. This is seen even for those flows which are clearly turbulent in nature. The absence of such effects can be illustrated by comparing the frames at $\omega t = 2n\pi$ and $2(n+1)\pi$, frames which show the flow structures at the start of successive cycles. In all cases, even the fine structure of the near wake flow can be seen to be replicated very clearly in these frames.

The second common feature of all the images is that the flows in the accelerating phases are quite different in form from their counterparts in the decelerating phases of the cycle, at the same instantaneous obstacle velocity. In this regard, the flows show hysteresis. For example, this characteristic may be seen in all sequences by comparing the flows at $\omega t = 2n\pi + (\frac{1}{2}\pi)$ (second in sequence) and $2n\pi + (\frac{3}{2}\pi)$ (fourth in sequence), where the instantaneous velocity in both phases is u_0. In this respect, such different effects of acceleration and deceleration upon the flow behaviour were also reported by Boyer *et al.* (1989 *b*, 1990) for unsteady rotating homogeneous flows.

(*ii*) *Lee waves*

Throughout several of the following sequences, internal waves are seen to be generated by the motion of the cylinder through the stratified fluid. The phase

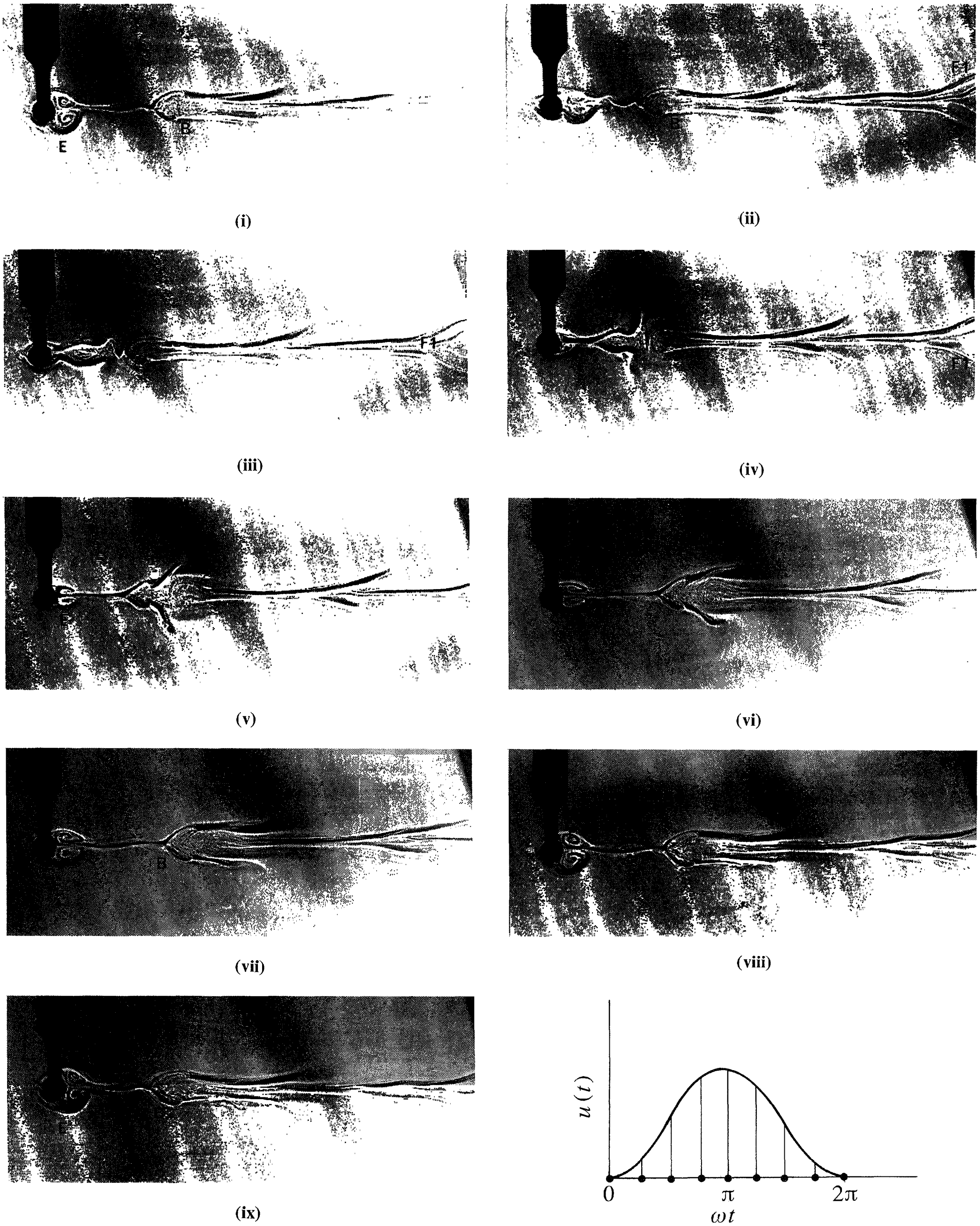

(i) (ii) (iii) (iv) (v) (vi) (vii) (viii) (ix)

Figure 2. Sequence of photographs taken at phases ωt: (i) $2n\pi$, (ii) $2n\pi + (\frac{1}{4}\pi)$, (iii) $2n\pi + (\frac{1}{2}\pi)$, (iv) $2n\pi + (\frac{3}{4}\pi)$, (v) $2n\pi + \pi$, (vi) $2n\pi + (\frac{5}{4}\pi)$, (vii) $2n\pi + (\frac{3}{2}\pi)$, (viii) $2n\pi + (\frac{7}{4}\pi)$, and (ix) $2\pi(n+1)$ within a single oscillation cycle, for $Re = 159$, $Fr = 0.61$, $\Theta = 0.58$, $\Phi = 1$, and $d/H = 0.11$. Type 2 flow.

surfaces of these waves are shown clearly by the dark and light patterns in the shadowgraph images. In this regard, it is pertinent to refer again here to the results of Stevenson & Thomas (1969) and Stevenson (1973), who were able to predict successfully the phase configurations of the internal waves formed by travelling oscillatory forcing effects.

For such cases, the regions in which waves are found are given by Lighthill's (1967) radiation condition, and, for purely horizontal motion, Stevenson & Thomas (1969) and Stevenson (1973) have shown that the following rules apply in the far-field for linear, two-dimensional, short-wavelength waves: in the first quadrant, waves are present for $\Theta < 1$ (in contrast to the steady case ($\Theta = 0$), where no waves are found). For values of the frequency ratio $\Theta > 1$, waves are found behind the body in a wedge-shaped region, with an included angle which decreases as Θ increases. (This latter circumstance contrasts with the pure oscillation case, where the St Andrew's cross wave pattern is generated only when the value of Θ remains less than unity.)

For comparative purposes, the theoretical relations derived by Stevenson (1973) have been used to compute phase configurations for those sequences exhibiting wave generation in the present study. Where appropriate, such computations are compared below with the shadowgraph data, to assess the importance in the present experiments of near-field processes (e.g. separation, large amplitude forcing) to the wave-field pattern. As in Stevenson (1969), only the first few waves of each family are shown.

(*b*) *Flow descriptions*

(*i*) *Flow types*

The illustrative sequences covered below by figures 2–13 represent the different principal flow types which were observed in the experiments. In the following section, these flows are classified to establish the form of the flow boundaries in $Re : Fr : \Theta$ parameter space, for constant Φ. In view of the rather complex changes which occur to the flow as these parameters are varied independently, the reader is directed to the summary classification shown later (figure 14) to appreciate more fully the inter-relation between flow types as they are described in turn.

1. *Type 1.* For sufficiently low values of Θ, the flows observed are, of course, very similar to the corresponding steady flow cases having the same values of *Re* and *Fr*. For this reason, full sequences are not presented here, though an example of one of these flows is shown in the summary régime diagram presented later in the paper in figure 14. In this example, for a case in which both *Re* and *Fr* take relatively low values, the characteristic phenomena of upstream blocking and attached flow seen (Boyer *et al.* 1989*a*) in the steady flow experiments are again observed. For these cases, the flow in the narrow rear wake of the cylinder is laminar, with the only contribution from the unsteadiness being the threaded appearance of the shadowgraph of the near wake region (see figure 14). Flow changes are insignificant throughout the forcing period, and there is good qualitative agreement between the wave structure shown in the shadowgraph images (figure 14) and the computed patterns of figure 15*a*.

2. *Type 2 (figure 2).* Figure 2 shows the detailed development of a type of flow in which the interaction of the gravitationally collapsing wake and the unsteady

Figure 3

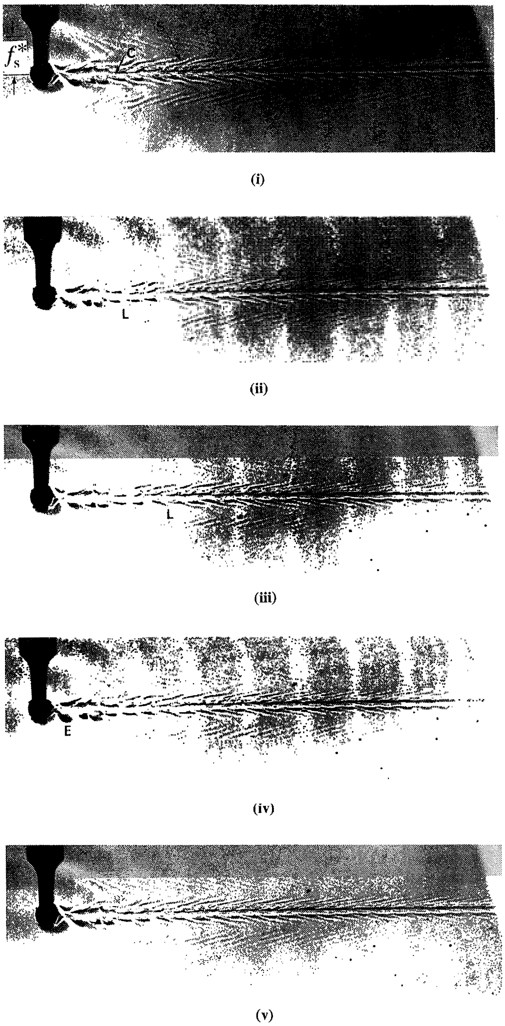

(i)
(ii)
(iii)
(iv)
(v)

Figure 4

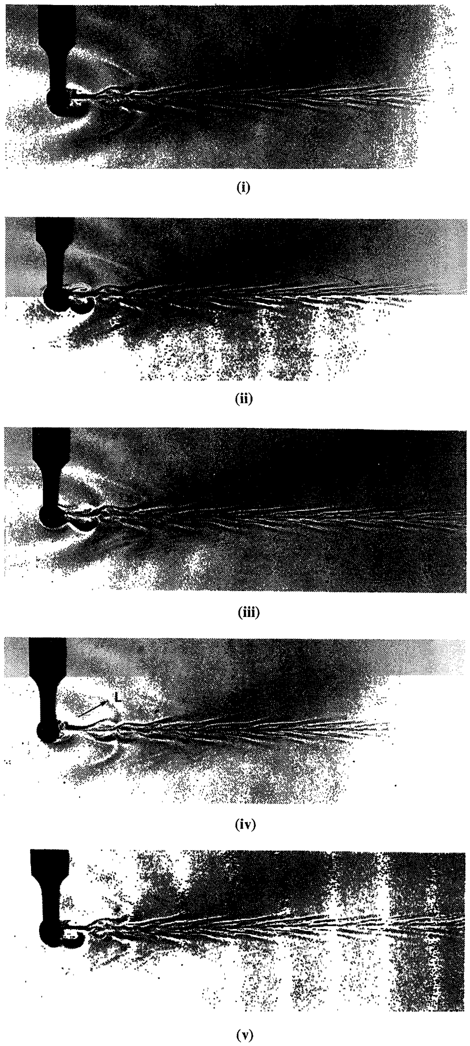

(i)
(ii)
(iii)
(iv)
(v)

Figure 3. Type 3 flow, showing predicted separation f_s^* of steady waves (see equation (4.1)). Same legend as figure 2, except $Re = 79$, $Fr = 0.23$, and $\Theta = 1.79$.

Figure 4. Type 4 flow. Same legend as figure 2, except $Re = 79$, $Fr = 0.24$, and $\Theta = 0.94$.

forcing of the flow is well demonstrated. In this case, nine frames per cycle are shown, to better delineate the complex flow development for this parameter combination. The schematic insert in this figure illustrates the positions in the cycle at which the nine frames were taken.

Throughout the maximum velocity and decelerating phases of the cycle (frames (v)–(ix)), the general structure of the wake is seen to consist of (i) a pair of counter-rotating eddies E attached to the rear of the cylinder, (ii) a bulbous head feature B in the intermediate wake region, and (iii) a sequence of bulges (the first of which is denoted F1) of fluid at several downstream locations. During the acceleration phase (frames (ii)–(iv)), the attached eddy pair is seen to be decoupled from the rear of the cylinder. In the intermediate wake, there are strong interactions during this phase between bulges generated in successive cycles. This is shown very clearly in frames (ii)-(vi) for the most recently generated bulge and its immediate predecessor, with clear evidence being shown of small-scale mixing occurring in the interaction region at the intruding bulbous nose of the collapsing bulge. The shadowgraph data indicate that within each of the bulges, the contained fluid has undergone mixing.

The period extending from $\omega t = \frac{1}{4}\pi$ before, to $\omega t = \frac{1}{4}\pi$ after the maximum velocity points ($\omega t = (2n+1)\pi$) is a convenient starting point to understand the flow development within a particular cycle. During this period (covered by frames (iv)–(vi)), attached eddies are generated by flow separation at the rear of the obstacle as the obstacle reaches, and then exceeds, the critical velocity at which eddies are generated. The size of the attached eddy pair E increases with increasing cylinder velocity (all other factors remaining constant), as for steady counterpart homogeneous and stratified flows (Taneda 1956; Boyer *et al.* 1989 *a*). During the deceleration phase $(2n+1)\pi \leqslant \omega t \leqslant 2(n+1)\pi$ of this cycle (for convenience, denoted the jth cycle), the rear wake fluid continues to be carried forward inertially as the cylinder is coming to rest, and the portion of dragged fluid closest to the body is then deflected vertically as it encounters the rear surface of the relatively slower moving cylinder. This interaction causes localized bulging of the eddy pair E, as shown clearly in frames (vi)–(ix). The height of the separation bubble pair E reaches its maximum value when the cylinder is instantaneously at rest, and, at this stage in the cycle, forward-moving wake fluid has overridden the stationary cylinder and has been advected past its leading surface (see frames (viii) and (ix)).

Since the transitions within each cycle are identical, it is convenient to follow the flow development to the $(j+1)$th cycle, by beginning the full sequence again at frame (i); i.e. the corresponding frame (ix) of the jth cycle). Thus, as the motion of the cylinder begins to accelerate again at the start of the $(j+1)$th cycle, the enlarged separation bubble containing low momentum fluid is shed from the rear of the cylinder at a time $\Delta t(\sim \pi/4\omega)$ into the cycle, and released from the cylinder as an isolated parcel of mixed fluid (see frame (ii)). Though the shed parcel then begins to undergo gravitational collapse (with an acceleration $N_{\mathrm{i}}^2 h_{\mathrm{i}}$, where h_{i} and N_{i} are the instantaneous values of the parcel height and buoyancy frequency respectively at a time t_{j+1} in the $(j+1)$th cycle, and $t_{j+1} = [(2(j+1)\pi/\omega) + \Delta t]$ after the start of the experiment), its collapse is interrupted by the longitudinal arrival of the relatively high momentum fluid still moving forward inertially in the lee of the cylinder. In consequence, the greater horizontal momentum of the forward moving fluid causes it to intrude into, and mix with, the recently generated and stationary separated parcel of mixed fluid at the rear of the cylinder (frames (iii)–(vi)). The bulbous head feature B (see figure 2, frame (vii)) is thereby formed as a result of the interaction.

It is noted that the preceding description of the flow development began at this stage in the previous cycle (figure 2, frames (iv)–(vi)), and subsequent developments in the $(j+1)$th cycle merely replicate those already described for the corresponding period in the jth cycle. Flow features formed at corresponding stages of the previous cycles are also present downstream of the obstacle, though each is displaced downstream relative to its immediate predecessor because of the mean longitudinal translation $2\pi u_0/\omega$ of the obstacle over a given cycle. The vertical extents of these features at given downstream reference stations are successively reduced with increasing time, because of dissipation.

3. *Type 3 (figure 3).* Interactions between successive wake features are less clearly delineated at higher values of the frequency ratio ω/N, because the collapse of a single mixed region is at a proportionately earlier stage when the next mixed region is generated. (In this regard, note that the amplitude η of the cylinder oscillation is given by $\eta = u_1/\omega$, so that the distances between successive mixed regions reduce as the frequency ratio ω/N increases, for fixed N). This behaviour can be seen clearly in figure 3, where the far wake consists of a very narrow central mixed region C, along the upper and lower edges of which are found sequences of 'spikes' S arrayed in a regular herringbone pattern. Such spikes are formed from the mutual intrusive motions of adjacent individual mixed regions generated at the rear of the cylinder. In the near wake, there is little evidence of attached eddy pairs being formed at the cylinder, except during the acceleration and decelerating phases (frames (ii) and (iv)), though evidence of symmetrical shedding of eddies is noted (see E in frame (iv), for example) in the near and intermediate wake regions. The wake again seems to be laminar, as for Type 2 flows, and cowhorn lee waves L are again clearly observed in the shadowgraph images.

4. *Type 4 (figure 4).* Figure 4 shows a somewhat different flow type from that of the previous example, though only the parameter Θ has been reduced. The effects of decreasing the forcing frequency are seen to have been twofold: firstly, the narrow mixed region in the wake has disappeared (to be replaced by a chevron pattern K of symmetric spikes), and, secondly, the process of symmetric eddy generation and shedding at the rear of the cylinder is more clearly operative than in Type 3 flows. The wake region appears to be laminar, and lee waves L are generated, as for the other flow types discussed above.

5. *Type 5 (figure 5).* For this type of flow, the wake region consists of (i) a near-field portion, in which symmetric eddies are generated and shed at the rear of the cylinder throughout the forcing cycle, (ii) an intermediate region in which the eddies E are extended into tear-drop shapes T before coalescing as they collapse gravitationally, and (iii) a far field region of isolated bulges F of mixed fluid. Within the intermediate region, the tear-drop eddies maintain their integrity for considerable distances downstream, particularly at the upper and lower interfaces between disturbed and undisturbed regions of the flow. Interfacial spikes K of the kind observed earlier in figure 4 are again seen for the Type 5 flows here, and cowhorn lee waves localized at the spikes are again generated in the otherwise undisturbed fluid. Note that the vertical extents of the intermediate and far field wakes are considerably increased over those in the other preceding flow types.

6. *Type 6 (figure 6).* For this type of flow, symmetric tear-drop eddies E are again formed in the same way as for Type 5, but these eddies quickly lose their integrity within the intermediate wake region, where mixing and coalescence of successive eddy pairs occur. Strong bulge features F (see frame (iii)) are formed in the far wake, and the regular array of spikes K at the upper and lower edges of the intermediate and far wake regions serve to indicate the locations of cowhorn wave patterns L. Though the general appearance of the intermediate and far-field wake does not alter significantly within the forcing cycle, frames (i) and (ii) of figure 6 show clear evidence of the intrusion of collapsing fluid into newly

PHILOSOPHICAL TRANSACTIONS OF THE ROYAL SOCIETY A MATHEMATICAL, PHYSICAL & ENGINEERING SCIENCES

Figure 5

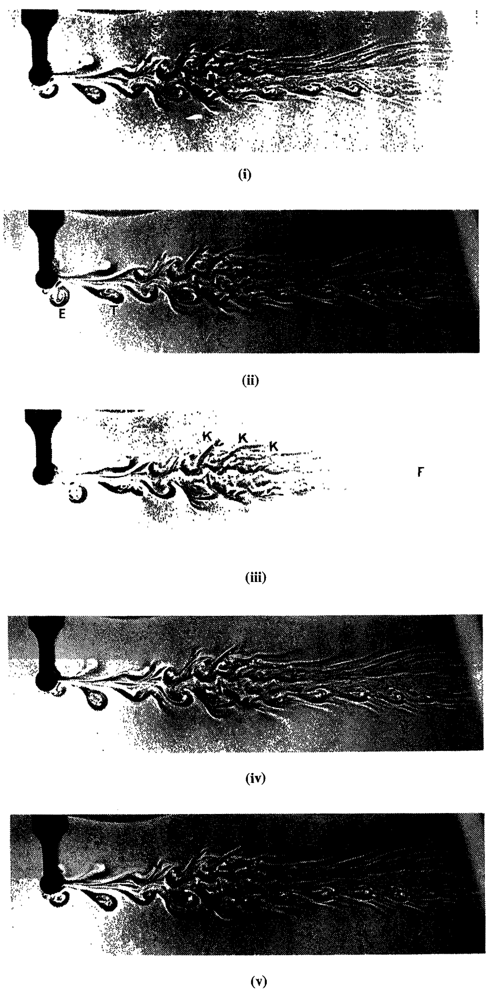

Figure 6

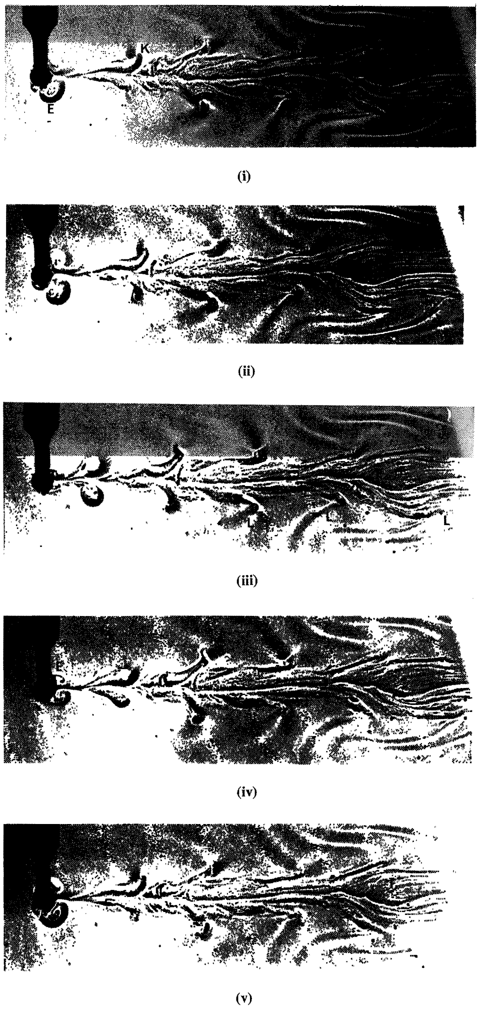

Figure 5. Type 5 flow. Same legend as figure 2, except $Re = 238$, $Fr = 0.96$, and $\Theta = 3.09$.
Figure 6. Type 6 flow. Same legend as figure 2, except $Re = 238$, $Fr = 0.69$, and $\Theta = 1.77$.

generated eddy patches, during part of the cycle. Within the collapsing region, internal wave motions can be seen.

7. *Type 7 (figure 7)*. Figure 7 shows that when the frequency of the motion is reduced from that of figure 6 (other parameters remaining fixed), the character of the near field wake flow is altered significantly. Eddies E are generated at the rear of the obstacle (see frame (ii)), but the eddies are now shed asymmetrically. For much of the forcing cycle, the flow within the whole wake region appears to be turbulent, and vigorous mixing takes place as successive collapsing patches interact and coalesce. The appearance of a knot-like feature N (see frames (iii) and (iv)) in the wake region intermediate to the asymmetric eddy field and the

Figure 7

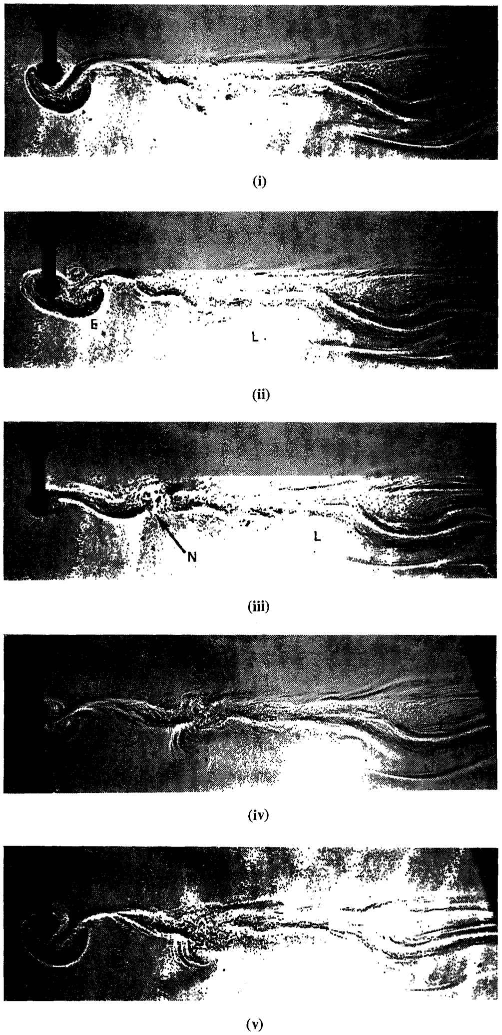

Figure 8

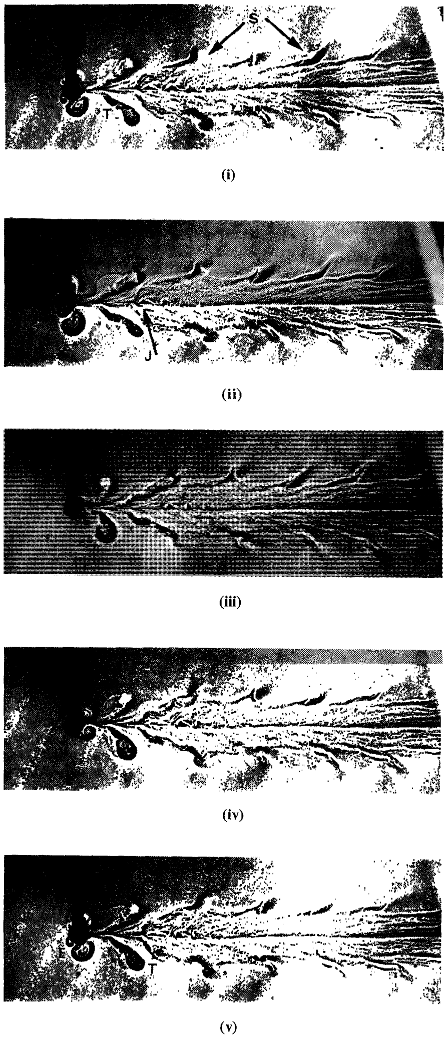

Figure 7. Type 7 flow. Same legend as figure 2, except $Re = 238$, $Fr = 0.73$, and $\Theta = 0.94$.
Figure 8. Type 8 flow. Same legend as figure 2, except $Re = 318$, $Fr = 0.93$, and $\Theta = 2.66$.

downstream bulges shows the intensity of this localized interaction. Cowhorn lee waves L are once more observed in the shadowgraph images, with their location being again indicated by the spikes or knot-like features in the intermediate wake.

8. *Type 8 (figure 8)*. For this type of flow, the relatively wide intermediate wake appears to be turbulent, with fine structure and approximately constant thickness throughout the forcing cycle. Tear-drop eddies T are again formed and shed asymmetrically from the rear of the cylinder, before being extended and collapsed to form the head J of the intermediate wake region (see frame (ii)). The signature of the periodic motion of the cylinder is again evident in the symmetric array of upper and lower spikes S, each of which is a site for the cowhorn wave

patterns observed for all $Fr \leqslant 1$ cases. A series of regularly spaced isolated bulges of mixed fluid is again formed in the far-field wake (i.e. to the right of the fields shown in the photographic frames), as shown in figure 7 for Type 7. Note also that a characteristic feature of the Type 8 flow (and certain of the other types described below) is the overshooting of the attached eddy pairs E when the cylinder is instantaneously at rest (frame (v)). This is seen particularly clearly in the lower of the two attached eddies of frame (i) in figure 8, where the steady flow shape of the eddy (as illustrated by frame (iv), for example) is distorted to a hook-like profile by the forward motion of fluid in the region very close to the cylinder surface.

9. *Type 9 (figure 9).* Figure 9 shows a different type of flow pattern (a 'Cobra eyes' pattern), which is generated at somewhat higher values of the Reynolds and Froude numbers than the case of figure 8, though at almost the same frequency ratio. Many of the same qualitative features of figure 8 are repeated here, though the formation of hook-like eddies O (see, for example, frame (ii)) at the cylinder surface at $\omega t = 2n\pi$ is more pronounced for the present flow type. This flow property leads to dramatic differences between the intermediate and far field structures of the two cases, as seen by comparing figures 8 and 9. It can be seen from such a comparison that the combined effects of increasing both Re and Fr have been (i) to increase the separation of individual mixed regions, and (ii) to cause the overshooting vortices at the cylinder to roll up in such a way that the expelled fluid feature contains a small double eddy pair W on the axis of the wake, and a pair of tear-drop-type eddies T at its edges (frame (i)). The small onaxis eddies are seen to persist as recognizable structures within the intermediate wake, throughout the forcing cycle.

10. *Type 10 (figure 10).* The flow parameters in figure 10 are identical to those in figure 8, except for the higher value of Fr in the former. However, the dramatic changes which are brought about by this difference are seen very clearly when comparing the two flow sequences. For Type 10 flows, the intermediate and far-field wakes are essentially unchanged in form throughout the forcing cycle, and there is evidence of small-scale mixing of fluid within these regions. The eddies E which are formed at the rear of the cylinder are shed symmetrically therefrom, and the shape of the collapsing eddy pairs C reveals the effects of overshooting of fluid during the decelerating phase of the motion. This effect (see frames (iv) and (v) of figure 10) is less pronounced than in the corresponding cobra eyes sequences (frames (iv), (v) of figure 9), but many of the flow details associated with this effect are to be seen in both cases. Note that for all phases except $\omega t = (2n+1)\pi$, the collapsing shed eddies within the near wake form a mixed patch region Q which is separated from the intermediate field. (This feature of the wake is accentuated in the next flow type.) As with the other flow sequences, figure 10 illustrates well the interaction of a collapsing newly generated mixed fluid patch with others generated at successively earlier times. This sequence of interaction events can be most easily appreciated by following the respective progress with time (starting at frame (i) in each case) of the eddy pair at the rear of the cylinder and the intermediate wake region downstream of it.

11. *Type 11 (figure 11).* The formation in the intermediate wake region of an isolated patch P of mixed fluid (which is separated as a distinct physical entity from the near field eddy pair feature G (frames (i), (ii), (v)) and the

Figure 9

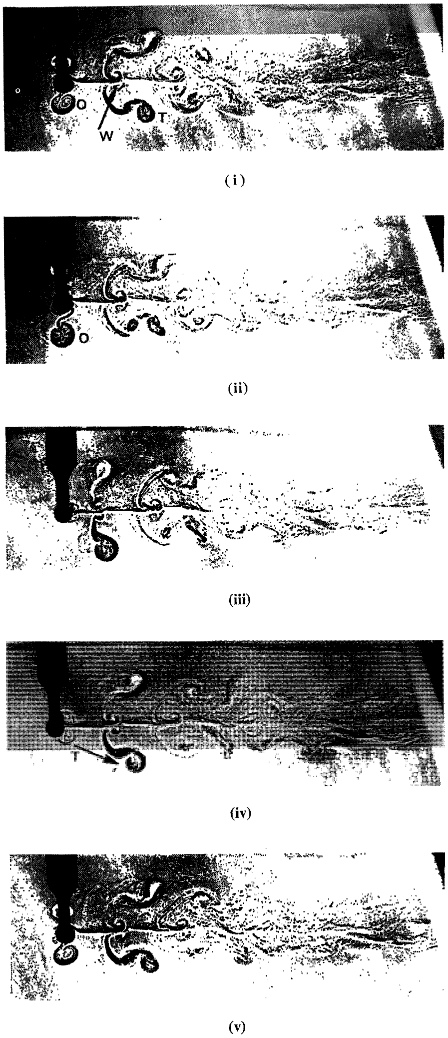

Figure 10

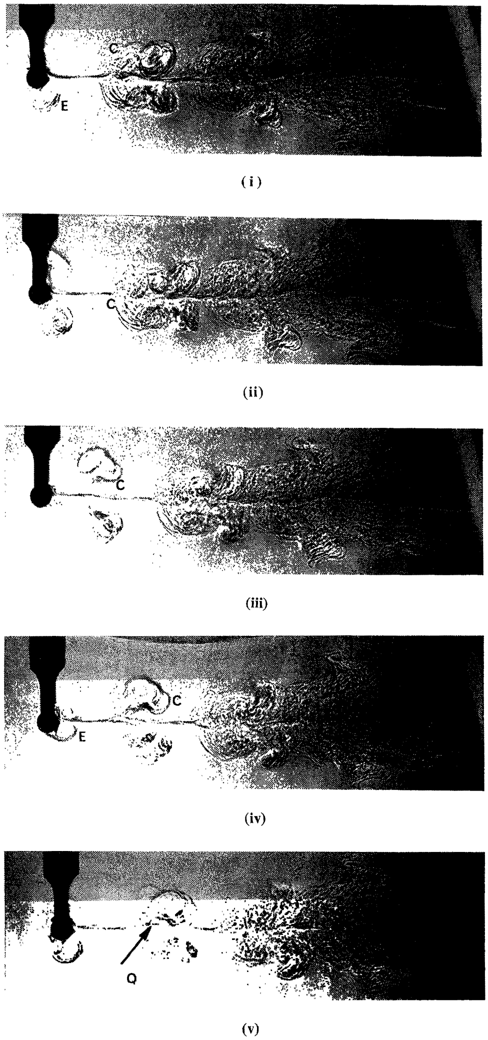

Figure 9. Type 9 flow. Same legend as figure 2, except $Re = 397$, $Fr = 1.59$, and $\Theta = 2.45$.
Figure 10. Type 10 flow. Same legend as figure 2, except $Re = 318$, $Fr = 1.37$, and $\Theta = 2.64$.

downstream bulges of mixed fluid M in the far-field) is the characteristic feature of this type of flow. As indicated in the legend to figure 13, such a patch is formed under the same circumstances of Type 10 flows, but for smaller forcing frequency ratios. Mixing takes place initially within the eddy pair which is (i) generated at the cylinder as a symmetrical attached eddy E (frame (iv)) and (ii) distorted into an overshooting feature G (frames (i) and (ii)) during the overshoot and shedding phases of the near-wake flow development. The subsequent collapse of the resulting mixed patch takes place separately from those of the corresponding patches generated during preceding cycles, and an isolated intermediate wake is generated. In the following cycle, this intermediate wake patch feature collapses further and interacts in turn with the corresponding patch generated one cycle

Figure 11

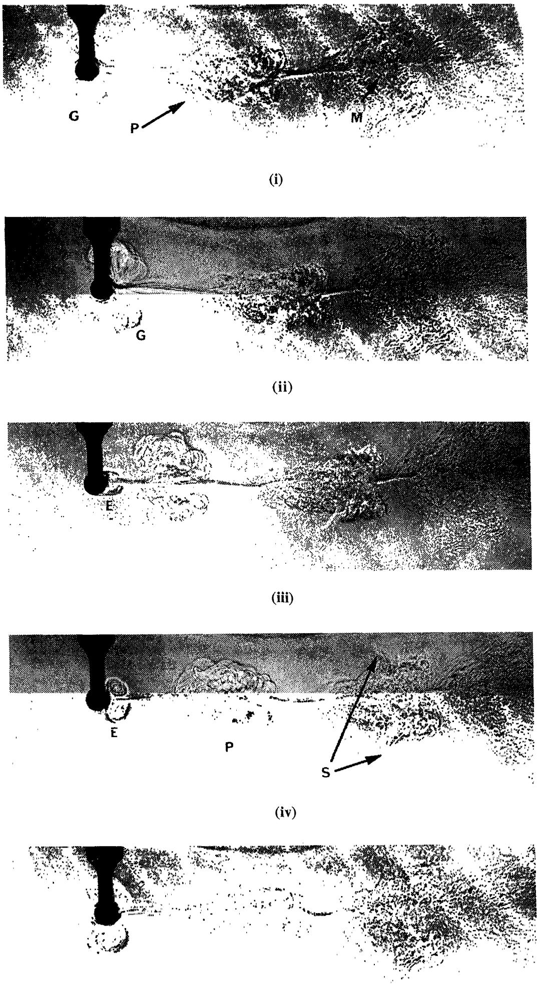

(i)

(ii)

(iii)

(iv)

(v)

Figure 12

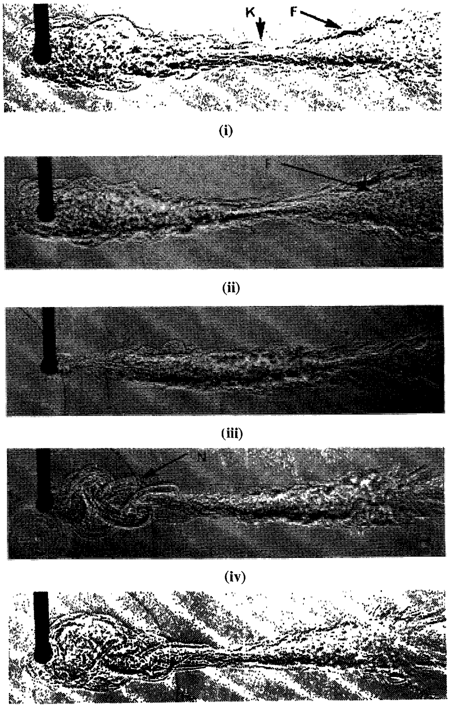

(i)

(ii)

(iii)

(iv)

(v)

Figure 11. Type 11 flow. Same legend as figure 2, except $Re = 318$, $Fr = 1.31$, and $\Theta = 1.90$.
Figure 12. Type 12 flow. Same legend as figure 2, except $Re = 381$, $Fr = 2.52$, and $\Theta = 0.94$.

previously. This latter interaction is manifested as a preferential intrusion of the older fluid patch into the more recently generated counterpart, and the consequent formation of a larger bulge of mixed fluid with a characteristic pair of spikes S (frame (iv)) locating the intrusion event.

12. *Type 12 (figure 12).* The formation of isolated bulges F of mixed fluid in the intermediate wake region (frames (i) and (ii), for example) is less clearly seen as the values of Re and Fr are increased and the value of Θ is decreased from those of figure 11. For this case, the appearance of the wake region varies significantly through the forcing cycle. There is no evidence of attached eddy pairs at the rear of the cylinder, though, during the deceleration phase, eddy shedding can be seen clearly within the structure of the near wake region N (see frame (iv)). Mixed

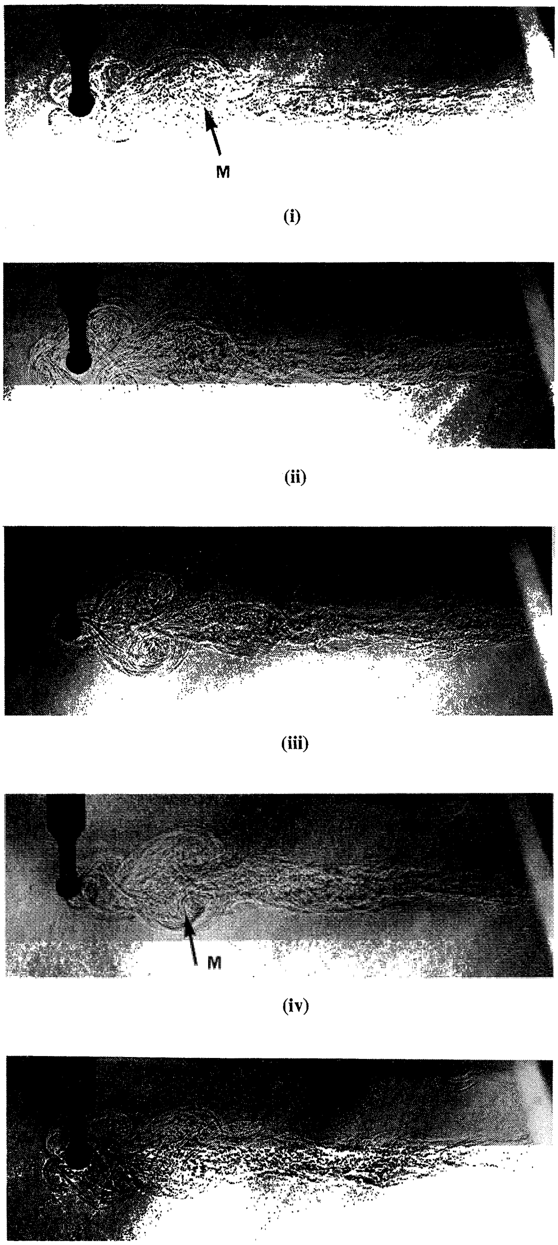

(i)

(ii)

(iii)

(iv)

(v)

Figure 13. Type 13 flow. Same legend as figure 2, except $Re = 397$, $Fr = 1.59$, and $\Theta = 1.84$.

fluid patches are seen to be generated in the far field throughout the cycle, but the near and intermediate regions of the flow are seen to change within the cycle from a fully turbulent narrow wake (frames (ii), (iii)), to a state where the large patch of mixed fluid which overshoots near the cylinder is separated from the far field bulges of mixed fluid (frames (i) and (iv) by a narrow intermediate knot K of mixed fluid.

13. *Type 13 (figure 13).* The flow parameters for figure 13 are identical with those of figure 9, except for the lower value of Θ in the former. This difference is seen to influence the flow appearance in a quite dramatic fashion. For this case, the near and far wake regions show fine structure, indicating the presence of turbulence and mixing, with a larger-scale symmetrical vortex pair being discernable within the single large mixed bulge M downstream of the cylinder (frames (i) and (iv), for example). This feature is recognizable throughout the forcing cycle. Significant overshooting occurs when the cylinder is instantaneously at rest, and the inertia of the overshooting fluid causes an increase in the upstream penetration of the mixed fluid for a short time into the acceleration phase of the cylinder motion. The width of the far wake region is considerably less than in earlier flow types, though far downstream a regular sequence of mixed fluid bulges is formed.

Figure 14 shows a three-dimensional summary plot of all data, with the régime locations appropriate to the above individual flow types being depicted by the symbols indicated. For comparison purposes, and to aid the interpretation of the figures, representative photographs for each flow type are shown for the phase $\omega t = 2n\pi$.

(ii) Lee waves

Figure 15 *a–e* shows the computed phase surfaces for the Type 1, 2, 3, 4 and 6 flow cases shown in summary form in figure 14. For the type of flow under investigation here, the principal features of the phase configuration diagrams are (i) the steady wave patterns, consisting of semicircles S_n radiating either upstream (e.g. figure 15 *a*) or downstream (e.g figure 15 *b–e*) from the obstacle, and (ii) the two families $F_{1,2}$ of waves associated with the periodic nature of the obstacle motion. The forms and spacings of the phase surfaces corresponding to these sets of waves can be compared with the shadowgraph images of the flow, since the latter contain information on the wave-induced distortions to the density surfaces. However, in this paper, the intention is not to attempt full quantitative comparisons between the computed and observed patterns, because of the following reasons: (i) in the near-field, the computed phase surfaces have validity only for linear disturbances from small amplitude motions—a situation not satisfied in the experiments, where large amplitude forcing takes place and where flow separation in the near field is common, (ii) the experimental flows have associated with them significant near-field mixing, so that the local values of the buoyancy frequency N (required for the phase configuration computations) are not known in the source region, and (iii) in contrast to the schlieren technique, the shadowgraph method (which relates intensity variations in the image to second-derivative density fluctuations in the flow) is not particularly well suited to the detection of phase surfaces (Davies 1992).

In spite of these deficiencies and incompatibilities, some comparisons are possible in the farfield regions of the computed and observed flow patterns. For example, the computed pattern of figure 15 *a* shows all of the principal features of the upstream influence and downstream distortion seen in the corresponding shadowgraph image in figure 14 for the quasi-steady case depicted as Type 1 flow. The far-field steady wave patterns in figure 15 *b–e* also shows good qualitative agreement with their counterparts in figures 2–4 and 6, and, in addition, the dimensionless spacing f_s^* $(= f_s/d)$ of the steady phase surfaces in the flow

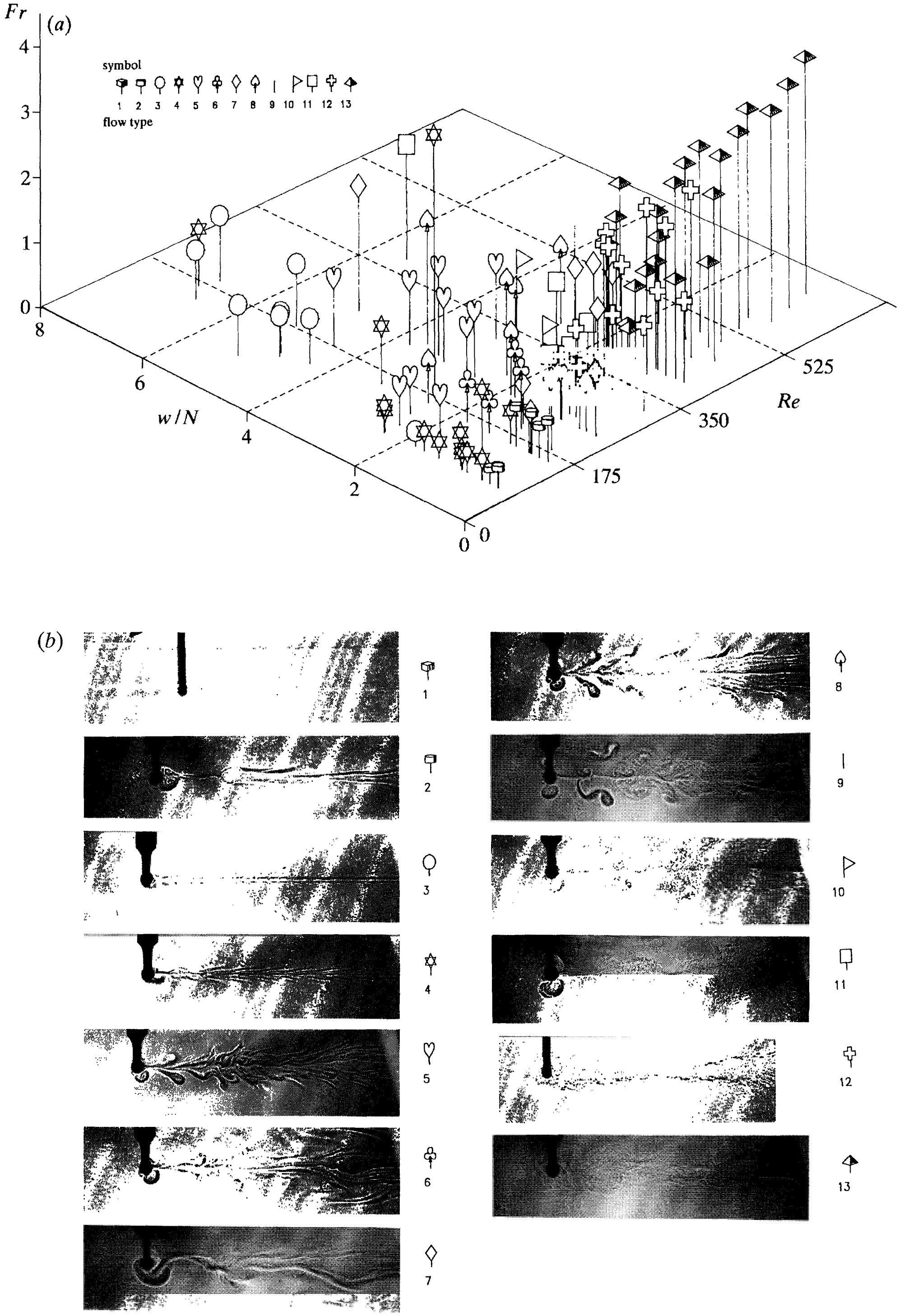

Figure 14. Three-dimensional ($Fr:\omega/N:Re$) régime diagram showing the occurrence of the flow Types 1–13 described in § 4 *b*. See attached key for identification and illustration of flow types.

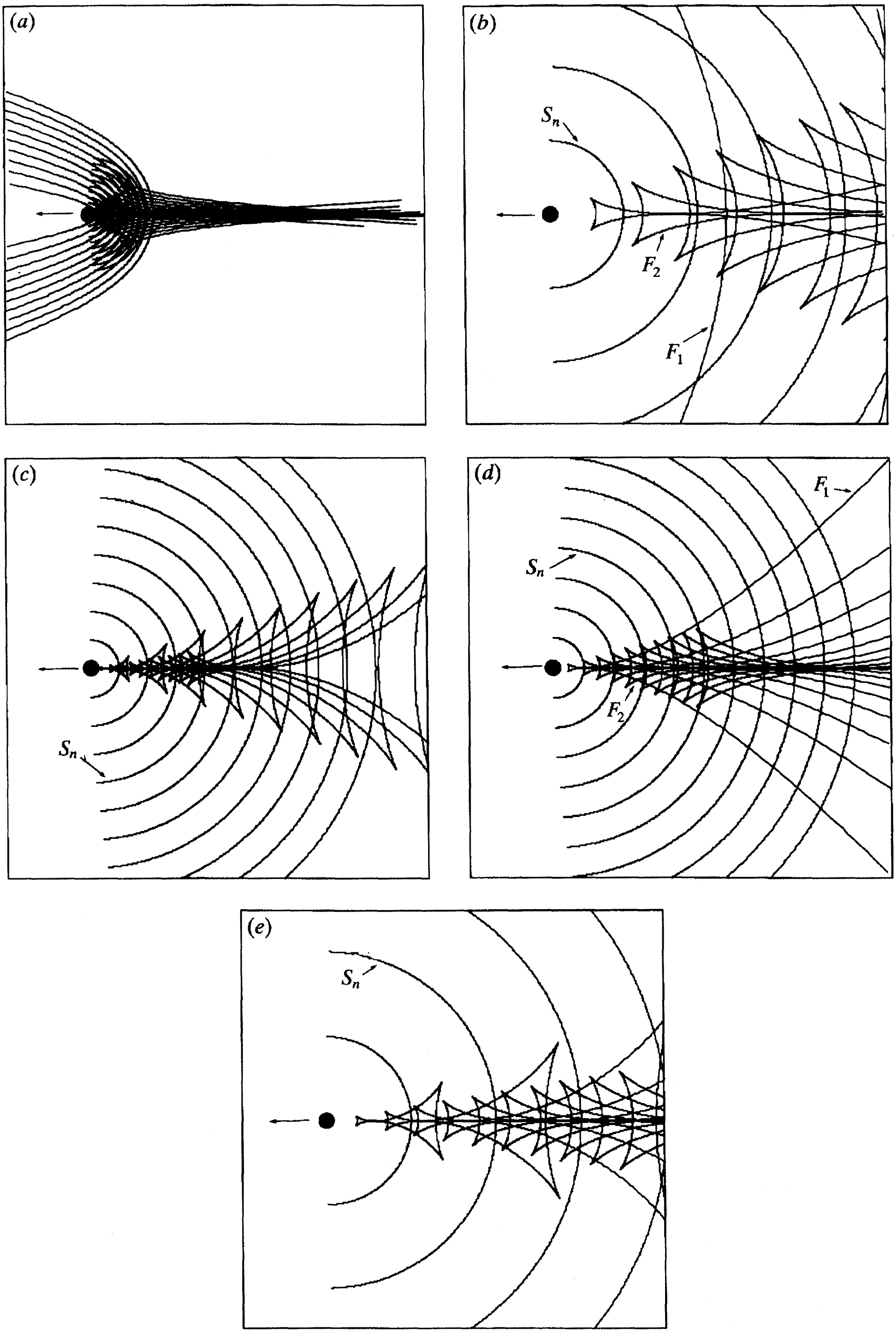

Figure 15. Computed phase configurations of the internal waves generated for the parameter values of the (*a*) Type 1, (*b*) Type 2, (*c*) Type 3, (*d*) Type 4, and (*e*) Type 6 images shown in figure 14.

visualization images accord well with the prediction,

$$f_s^* = 2\pi(Fr), \tag{4.1}$$

of theory (Stevenson & Thomas 1969). This comparison is shown for figure 3, one of the cases in which the shadowgraph image is relatively clear and for which the near-field distortion of the flow is minimal. The two sets of swept-back phase surfaces in the image sequence is associated with the unsteady motion of the body, and the shapes of these features are seen to show good qualitative agreement with the computed counterpart patterns in figure 15. Both sets of phase surfaces can be identified readily in the shadowgraph images (see, for example figures 3 and 4) corresponding to the cases of minimal near-field distortion, and the relative spacings f_u of the unsteady phase surfaces, as compared with those of the steady wave patterns are in good qualitative agreement with the predictions. Indications of the predicted local scales of f_s^* for the steady phase surfaces in figure 3 are shown directly on the figure. For the reasons given above, precise quantitative comparisons of the predicted and observed waves are not meaningful, particularly in the cases such as figures 2, 5 and 6 where the localized distortion of the flow field obscures the wave pattern. However, as shown above (particularly by figures 3 and 4), the comparisons of the steady and unsteady patterns show satisfying qualitative agreement between theory and experiment.

(*i*) *Far-field effects*

In the cases described above, attention has been concentrated primarily upon the structure of the near and intermediate regions of the wake. However, as indicated earlier, qualitative measurements of flow activity in the far-field have also been made. The most prominent features in the far field wake region are the isolated bulges formed at discrete locations downstream of the cylinder. The first of these ('F1') was identified earlier in figure 2 (frames(ii)–(iv)). The bulges are associated with mutual interactions in the intermediate and far-field between the periodically shed parcels of fluid described in the previous section for the near wake region. At a fixed point in the far-field wake, the bulges are seen to dilate and contract periodically, with the motion of adjacent bulges being in anti-phase with each other, and with the amplitude of the motion decreasing with time (i.e. distance downstream of the cylinder). In this regard, the time-dependent far-field motion resembles a damped solitary wave (see, for example, Maxworthy 1979; Koop & Butler 1981; Kao *et al.* 1985; and references therein). Figure 16*a* illustrates the far wake structure corresponding to the near-field images in figure 2(i) and (ix), and, for purposes of comparison, the remaining sketches in figure 16 illustrate the far-field structure for other exemplary flow types. Inspection of figure 16 and other flow visualization data reveal that the downstream bulges are common features of the far-field wakes for all of the flow types investigated. Note also the similarities in behaviour of these bulges and the counterpart features described by Boyer *et al.* (1989*a*) for steady forcing. For each case, the relative displacements of the bulges is regular with respect to the cylinder at each stage of the cylinder oscillation cycle, with the position and spacing of the bulges (and their amplitudes) being determined by the particular combination of Re, Fr and Θ under consideration.

PHILOSOPHICAL TRANSACTIONS OF THE ROYAL SOCIETY A MATHEMATICAL, PHYSICAL & ENGINEERING SCIENCES

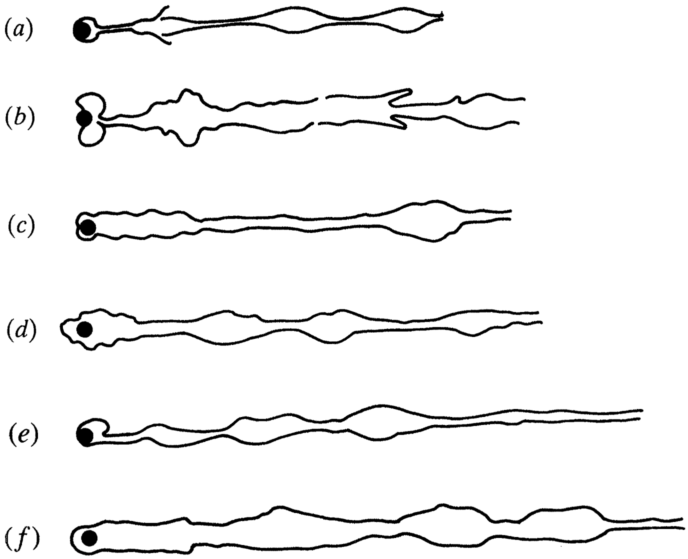

Figure 16. Sketches derived from composite photographs, showing far wake structures for [Re : Fr : Θ] values of (*a*) [159:0.59:0.86] (Type 2 flow), (*b*) [238:0.88:1.14] (Type 11), (*c*) [318:1.18:0.57] (Type 13), (*d*) [318:1.21:0.88] (Type 12), (*e*) [318:1.19:1.15] (Type 7), and (*f*) [238:0.95:0.92] (Type 12), for $\omega t = 2n\pi$.

(*c*) *Scaling considerations*

(*i*) *Overshooting*

As indicated above, upstream overshooting of the cylinder by downstream fluid is a common occurrence for certain parameter ranges, with fluid in the rear wake of the cylinder moving forward with a velocity which is greater than that of the cylinder at certain stages of the forcing cycle. For some parameter combinations, the effect is most apparent (see, for example, figures 7, 9 and 11) when the obstacle is instantaneously at rest ($\omega t = 2n\pi$, $n = 0, 1, 2 \ldots$), but it can also be seen when the cylinder has started moving at the beginning of the acceleration phase (see, for example, figures 12 and 13, frames (ii)). The mechanisms responsible for the overshooting phenomenon may be understood by considering the acceleration scales present in the flow, as follows.

The first cases are those for which the values of the Reynolds and Froude numbers are sufficiently low for the flow to be laminar and for the flow to be influenced significantly by viscous diffusion effects. (It is noted that such cases lie outside the parameter ranges investigated herein and that here they are of academic interest only, but it is instructive to consider them briefly for completeness and for comparisons with future measurements.) Here, deceleration of the solid surface of the obstacle causes a viscous stress to be transmitted from its solid surface to all regions of the surrounding fluid, including those regions initially at levels above and below the levels occupied by the cylinder. The typical viscous response time for fluid particles at distance l above or below the cylinder surface is l^2/v, and the associated viscous diffusion velocity u_e and acceleration a_e are given by

$$u_e = (v/t)^{1/2}, \quad a_e = (v^{1/2}/t^{3/2}), \tag{4.2}$$

respectively. Over a single period of oscillation of the obstacle, a_e is $O(v^{1/2}\omega^{3/2})$. The deceleration a_c of the cylinder itself is $O(u_0\omega)$, so that if $a_c \geqslant a_e$ overshooting will be expected to occur, at least at levels above and below the level of the cylinder. The value of the dimensionless ratio $B = (a_c/a_e)^2 = u_0^2/v\omega$ can then be regarded as an indicator of the likelihood of overshooting, with high values of B favouring the occurrence of the phenomenon.

Fluid particles initially in the downstream wake are forced to move vertically as they are carried forward and collide with the rear of the instantaneously stationary cylinder. Because of their buoyancy, such particles experience a restoring force as they are deflected vertically. For these particles, the important ratio determining their subsequent motion is that between the acceleration of the obstacle at the start of the cycle and the restoring acceleration N^2d. Thus, the prevention of overshooting as a result of gravitational collapse will occur for such particles if the ratio $R = N^2d/u_0\omega$ is less than some quantity of order unity. Particles are then able to surmount the obstacle and undergo further vertical excursions before the motion of the latter resumes.

For the cases investigated here, in which viscous diffusion effects were negligible, fluid within the wake is dragged inertially in the direction of motion of the obstacle, and the overshooting which is then observed is due solely to this process (as with a homogeneous fluid). Fluid motions are then affected significantly by the inertial acceleration, with the drag force per unit mass exerted on the fluid being $O(u_0^2/d)$. In these cases, the relevant condition to be satisfied for overshooting is

$$u_0^2/d \geqslant a_c, \tag{4.3}$$

i.e. the parameter $K_0 = u_0/d\omega$ is greater than unity. For cases of turbulent flow in which both buoyancy and inertial effects are significant, effects of K_0 (and hence K, in these cases) can therefore be expected to dominate the flow behaviour if $u_0^2/d \gg N^2d$ (i.e. $Fr^2 \gg 1$).

From the above discussion it is clear that for the experiments conducted, the criteria for overshooting are simply that the values of the acceleration ratio R and the parameter K_0 should both exceed critical values. These criteria are investigated further below.

Figure 17 summarizes the data collected on the overshooting behaviour. Following the scaling considerations above, the data are classified into separate flow régimes as follows according to the degree of overshooting experienced.

Régime 1. At some stage in the forcing cycle, the rear wake fluid washes completely past the cylinder in the manner of, say, figure 13(i), (ii) and (v).

Régime 2. At some stage in the forcing cycle, wake fluid moves forward with respect to the cylinder, with a typical maximum relative excursion of one cylinder diameter. An example of this behaviour is given by figure 11(i) and (ii) and figure 8(i) and (ii).

Régime 3. No overshooting.

In figure 17, the overshooting data are shown with the inverse acceleration ratio $R = u_0\omega/N^2d$ as abscissa, and the parameter $K_0 = u_0/d\omega$ as ordinate. It is noted that the product of R and K_0 is simply the square of the Froude number Fr, so the critical condition of $Fr = 1$ (see below) is represented on the régime plot of figure 17 by a hyperbolic curve.

The régime plot shows significant clustering of data types within clearly delin-

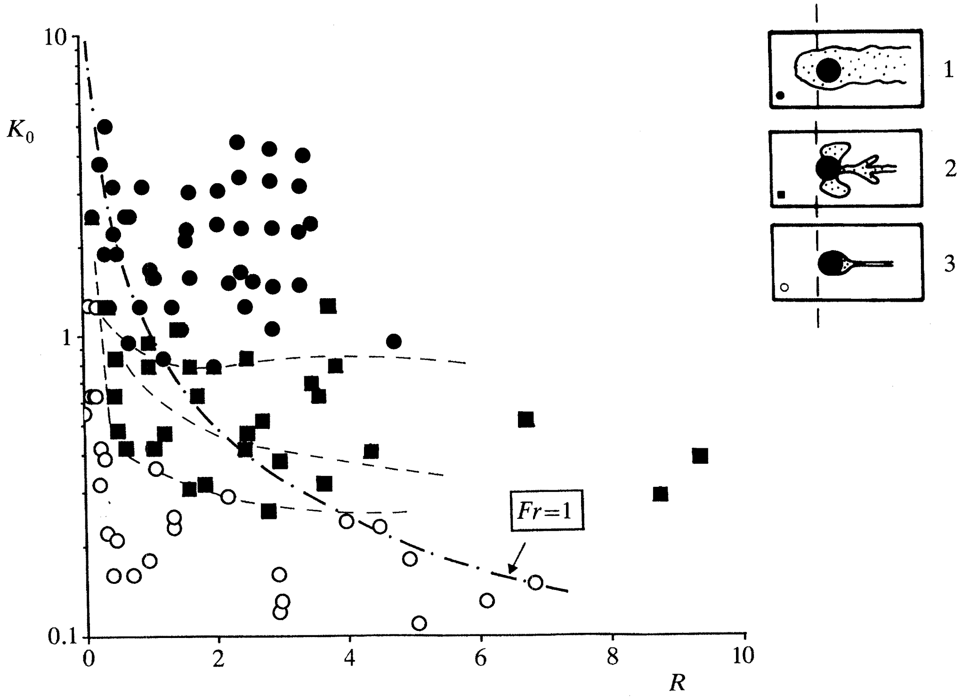

Figure 17. Flow régime plots of $K_0 = u_0/d\omega$ against $R = u_0\omega/N^2d$, for overshooting régimes 1 (•), 2 (■) and 3 (○).

eated boundaries, and it is noted for very low values of R, the [Régime 3→Régime 1] transition is accomplished without the flow displaying the intermediate stages typified by régime 2. For sufficiently high (not less than 1.5) values of K_0, there is strong overshooting (i.e. régime 1 flow) for all values of R; this bounding value of 1.5 corresponding in the experiments to a value of Re of just less than 300.

The data shown in figure 17 confirm the validity of the scaling arguments outlined above, namely that inertial overshooting effects are favoured by the condition that $u_0^2/d \gg N^2d$ (i.e. $Fr^2 \gg 1$). Figure 17 illustrates that this condition is generally satisfied well for both régime 1 and régime 2 flow, the flow types with the strongest manifestations of inertial overshooting. The curve delineating the $Fr > 1$ and $Fr < 1$ conditions is seen to separate quite well the data points corresponding to the most extreme flow régimes (3 and 1 respectively), and the overshooting régime 2 is also well-described by the Froude number classification. The individual data-sets shown on figure 17 also confirm the earlier proposition that high values of K_0 are associated with the overshooting phenomenon. For values of R greater than about 1, the full set of transitions between régimes 3 and 1 are observed as the values of K_0 are increased.

(*ii*) *Wake flows*

For cases in which overshooting does not occur, the significant changes which take place as the frequency ratio is changed are localized to the downstream wake. Then, an important question to be addressed is whether the flow which is observed at any instant within one oscillation cycle is representative of the steady flow associated with the appropriate instantaneous Reynolds and Froude numbers of the flow (as summarized in the flow régime diagram of Boyer *et al.* (1989 *a*). If this is not the case, phenomena associated specifically with the time-dependence of the forcing can be anticipated.

Conditions for the occurrence of these new phenomena can be gauged in the following manner, by considering the extreme cases of buoyancy-dominated ($Fr \ll 1$) and inertia-dominated ($Fr \gg 1$) flows. In both cases, the respective conditions to be satisfied for the 'new' phenomena to occur are that the relevant buoyancy or inertial adjustment times of the flow should be long compared with the period of oscillation of the obstacle. Conversely, if the flow adjustment time is relatively short, no significant effects of oscillation frequency can be expected at a given stage in the oscillation cycle.

For the buoyancy-dominated régime ($Fr \ll 1$), the relevant adjustment time is N^{-1}, so that specific effects of obstacle oscillation are anticipated only when the frequency ratio ω/N exceeds a critical value. For the inertia-dominated régime ($Fr \gg 1$), the adjustment time is simply the advective scale d/u_0, and the relevant condition for frequency effects to be significant is that the ratio $u_0/d\omega$ (the parameter K_0) is much less than some critical value. The latter ratio may be rewritten in terms of Fr as

$$K_0 = u_0/d\omega = Fr/\Theta, \tag{4.4}$$

so that, for this régime (where $Fr \gg 1$), the value of the frequency ratio Θ at which effects of unsteadiness will be observed will be dependent upon the Froude number of the flow. Specifically, as the value of Fr increases, new phenomena will only be expected if Θ assumes progressively greater values to ensure that the ratio Fr/Θ remains less than unity. Figure 18 *a* shows a schematic representation of this effect, with the solid curve delineating the simultaneous limiting conditions:

$$Fr/\Theta = 1, \quad \Theta > 1 \tag{4.5}$$

for the occurrence of new phenomena.

Figure 18 *b* uses the framework of figure 18 *a* to show a scatter plot for the occurrence of the 13 flow types described above in § 4 *a*(*ii*) and classified in figure 14. There are a number of points of interest which arise from such a representation, particularly with regard to the preceding discussion. Firstly, for example, it can be seen that the diagram serves as a convenient régime classification plot for several flow types (Types 2–6 and 8) which each cluster conveniently within well-defined $\Theta : Fr$ parameter boundaries. This is a somewhat unexpected result, since the plot of figure 18 is a two-dimensional representation of a three parameter problem (see figure 14). Secondly, it can be seen that these identifiable groupings (except for Type 2 flows) occupy regions of $\Theta : Fr$ parameter space which satisfy the joint conditions (see (4.5) above) for the occurrence of flow phenomena associated specifically with the unsteady nature of the forcing. Likewise, parameter combinations not satisfying condition (8) are not well classified by the plot of figure 18 *b*, as illustrated by the non-systematic distributions of flow Types 7, 11, 12, and 13 in particular, for $Fr > \Theta$. It is noted that these flows all correspond to cases in which the wake flow is turbulent, and all cases correspond to relatively high values of the Reynolds number Re (see figure 14). Within this régime, the classification of the flow is clearly determined by the values of all three controlling dynamical parameters, and not two as for the cases above.

If attention is directed at the flow types which lie within the $Fr > \Theta$ portion

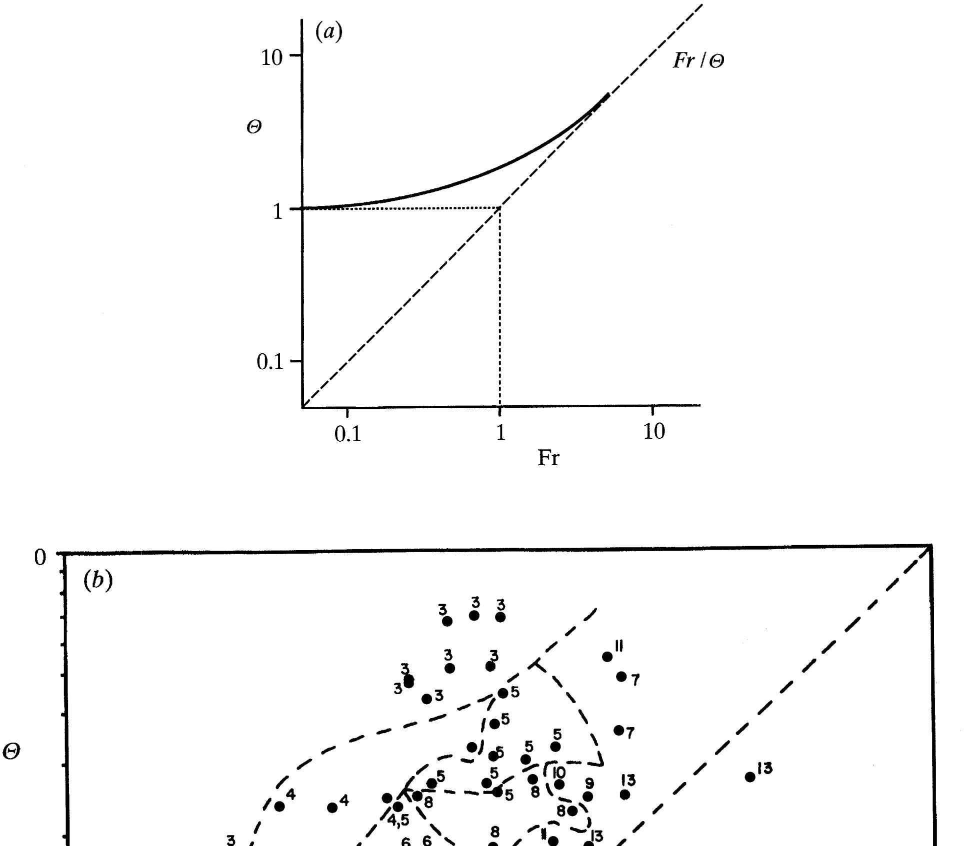

Figure 18. Plots of Θ against Fr showing (a) schematic representation of conditions ($Fr/\Theta < 1 : \Theta > 1$), and ($b$) distribution of flow Types 2–13.

of figure 18, it is noted that it is these flow types which most clearly illustrate the flow development taking place in a sequence of quasi-discrete steps, for each of which the flow resembles instantaneously that which would be observed for steady forcing at the same instantaneous values of both Fr and Re. This behaviour can be seen, for example, in figure 12 for Type 12 flow, where both 'turbulent symmetric' and 'vortex shedding laminar' flow types (Boyer *et al.* 1989 *a*) are observed instantaneously (frames (iii) and (iv) respectively) as the velocity of the obstacle decelerates. Reference to the régime diagram of Boyer *et al.* (1989 *a*) confirms that these are the T_{S} and V_{L} flows to be expected for the instantaneous $[Re : Fr]$ combinations of [762:5.04] and [381:2.52] respectively appropriate for these frames in the sequence.

The plot on figure 18 *b* illustrates that the cases which best satisfy the two simultaneous conditions ($Fr/\Theta < 1$; $\Theta > 1$) for the appearance of 'new' flow structures, quite distinct from those associated with steady forcing, are those denoted 3, 4, 5, 6, 8, 9, 10 and 11. Reference to the sequences of shadowgraph images and accompanying flow descriptions (§ 4 *a*(*ii*)) for these types confirms the general predictions of the above model. In all of these examples, the wake flow contains characteristic features ('chevrons', 'spikes', 'cobra-eyes', for example) which are not seen for cases in which the motion of the cylinder is steady.

(*d*) *Quantitative measurements*

For flows in which the rear wake was turbulent (flow types denoted 7, 11, 12 and 13 in the classification of figure 14 and the accompanying descriptions of § 4 *a*(*ii*)), measurements were made of the dimensions of the wake and the degree of forward overshooting for the full range of conditions. One of the primary purposes of this procedure was to reveal the effects of unsteadiness in the present experiments by comparing the wake dimension data with measurements from the previous counterpart investigations (Boyer *et al.* 1989) with steady flow forcing. In such a way, the effects of unsteadiness on some geometrical aspects of the flow structure could be gauged.

The observables adopted for (i) the comparison of the wake dimension data and (ii) the quantification of the degree of forward overshooting were the maximum dimensionless vertical width $\gamma^* = \gamma_{\max}/d$ and the maximum forward excursion $\epsilon^* = \epsilon_{\max}/d$, respectively, during one forcing cycle (see figure 19 for a defining sketch).

As indicated in § 4 *b*(*i*), the maximum values of γ and ϵ did not always occur in phase with (i) each other, and (ii) a particular stage in a given each cycle, so it was necessary to monitor the variation in both quantities throughout several cycles to determine γ^* and ϵ^*. Typical results of this monitoring procedure for intervals of between two and three cycles are shown in figure 20 *a*–*d*. These plots illustrate and confirm the discordance in some cases between the times at which the maximum values of both γ and ϵ occur and, for example, the $\omega t = 2n\pi$ values for which the cylinder is instantaneously at rest. Also, the data illustrate the phase differences between the variations of γ and ϵ with time, for representative flow examples. This effect is particularly noticeable in figure 20 *b*, where the variations in γ and ϵ occur with a phase difference of between $\frac{3}{4}\pi$ and π.

Using time records such as those presented in figure 20, values of γ^* $(= \epsilon_{\max}/d)$ and ϵ^* $(= \epsilon_{\max}/d)$ have been measured (for turbulent wake flows only), and plotted in terms of the relevant forcing parameters. The results of the overshooting

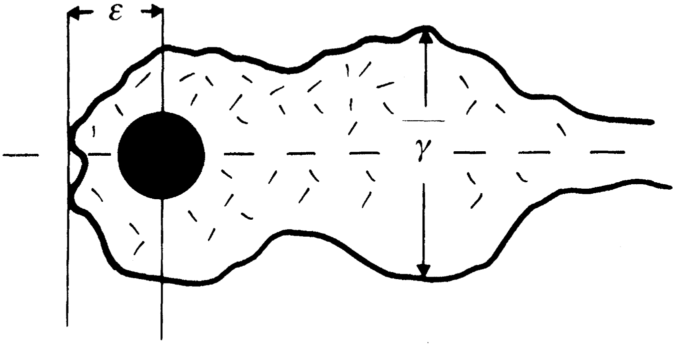

Figure 19. Schematic diagram showing the instantaneous wake flow for Types 7, 12 and 13, and the definition of the quantities γ and ϵ.

flow classification above indicate that the most important dimensionless parameter controlling the occurrence of the overshooting phenomenon (and, by implication, the degree of overshoot) is likely to be the parameter K_0, and that the roles of the parameters $B(=u_0^2/\nu\omega)$ and $R(=u_0\omega/N^2d$ are less significant for this aspect of the flow. That is, the forward overshooting process of the turbulent wakes does not seem to be controlled by buoyancy constraints. Accordingly, ϵ^* data for all flow types associated with turbulent wakes have been plotted against K_0 (see figure 21). The data show quite good agreement with the scalings developed above, in spite of the scatter which becomes more acute at higher values of K_0. It is noticeable that the dependence of ϵ^* upon K_0 becomes weaker beyond $K_0 \approx 3$, as the value of the forcing frequency decreases for fixed values of the mean velocity u_0 and cylinder diameter d.

Figures 22 and 23 summarize the behaviour of the maximum width of the turbulent wake, as the external forcing parameters are varied. For cases of steady motion of a cylinder in a stratified fluid, previous experiments (Boyer *et al.* 1989) confirm that the maximum wake width scales with $Fr^{1/2}$, and it is with this result that the present data may sensibly be compared, if effects of unsteadiness alone are to be detected. The plot is shown in composite form in figure 22, for all values of the parameter $\Theta(=\omega/N)$ and for all relevant flow types (see figure 21). The data show good qualitative agreement with the $Fr^{1/2}$ dependence, implying that effects of unsteadiness (at least, as they enter through variations in Θ) are not significant for this property of the near field wake flow. This result is confirmed by the plot of figure 23, where the lack of dependence of γ^* upon the frequency ratio Θ is shown for bands of values of Fr. It can be seen that the trend of the data in both figures 21 and 22 are consistent with a principal dependence of γ^* upon $Fr^{1/2}$, and no significant dependence upon Θ.

Though the data in figure 22 satisfy very well the $Fr^{1/2}$ dependence established by Boyer *et al.* (1989 *a*) for steady forcing, there remains a quantitative discrepancy between the two data-sets. Specifically, the best linear regression fit to the present data,

$$\gamma^* = 4.34(Fr^{1/2}) - 0.76 \tag{4.6}$$

(with a coefficient of determination of 0.85) produces dimensionless maximum

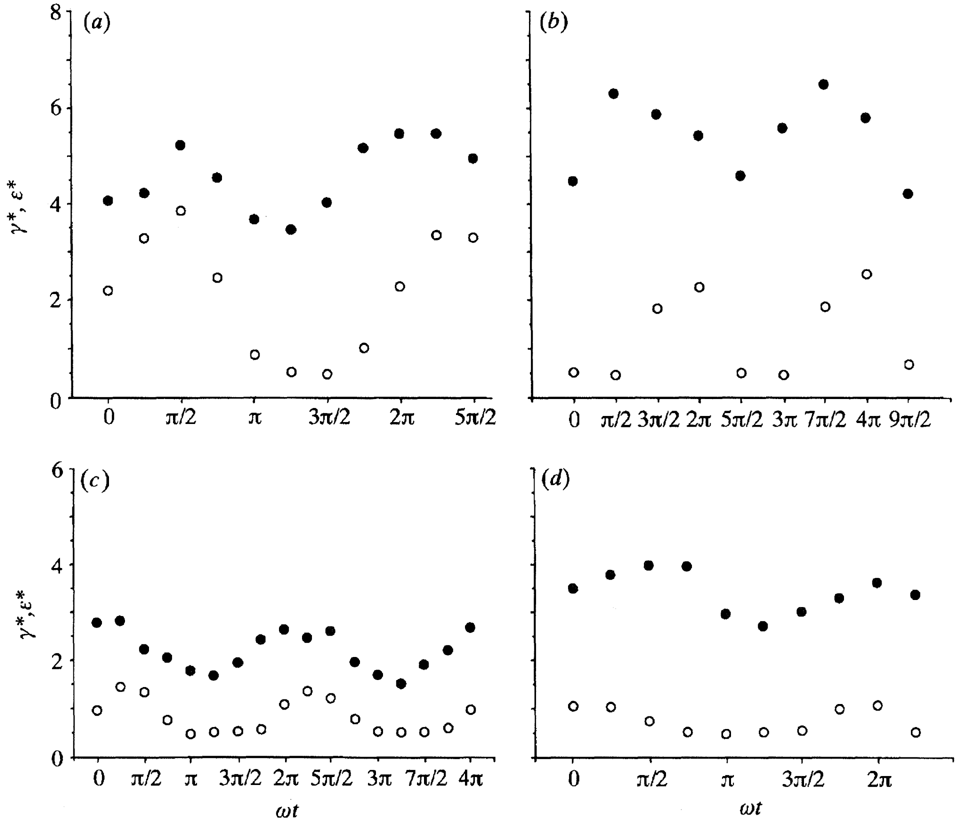

Figure 20. Composite plots showing variations with time of γ^* and ϵ^*, for $\Phi = 1$ and [$Re : Fr : \Theta$] values of (*a*) [397:1.67:0.96], (*b*) [610:3.48:0.83], (*c*) [238:0.73:0.94], and (*d*) [476, 1.38:1.77].

wake widths which are systematically and significantly greater than those

$$(\gamma^*)_\mathrm{m} \approx 2.4 Fr^{1/2} \tag{4.7}$$

obtained by Boyer *et al.* (1989 *a*) for otherwise identical steady forcing conditions, regardless of the value of the forcing frequency Θ. This comparison is shown directly on figure 22.

This somewhat surprising result can be clarified, if it is noted that the values of Fr in the comparison between the steady and unsteady cases are both computed using u_0 as the velocity scale. However, for the type of unsteady motion under consideration here, the velocity of the cylinder varies within a cycle, and it reaches a maximum instantaneous value of $2u_0$ at the phase value of $\omega t = (2n+1)\pi$. Thus, providing that the conditions described in § 4 *b* are satisfied, the instantaneous maximum wake width $(\gamma^*)_\mathrm{i}$ will vary through the cycle, with the maximum value γ^* being correlated *a priori* with the maximum velocity of the cylinder. That is, it will be determined by $(Fr_\mathrm{i}^{1/2})_\mathrm{max}$, the instantaneous maximum value of $Fr^{1/2}$ based upon an instantaneous maximum velocity $2u_0$. The chain-dashed line in figure 22 shows the effect of redefining Fr in terms of this velocity, and thereby readjusting all abscissa values by a factor $2^{1/2}$; as a consequence of this redefinition

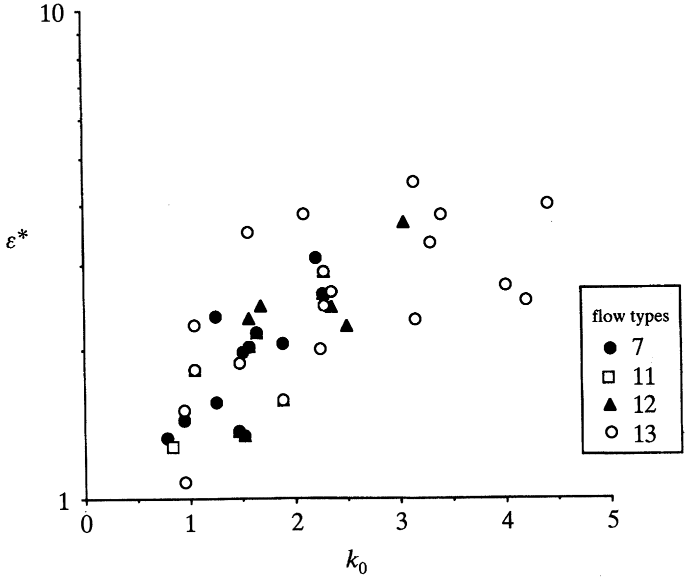

Figure 21. Composite plot of ϵ^* against K_0.

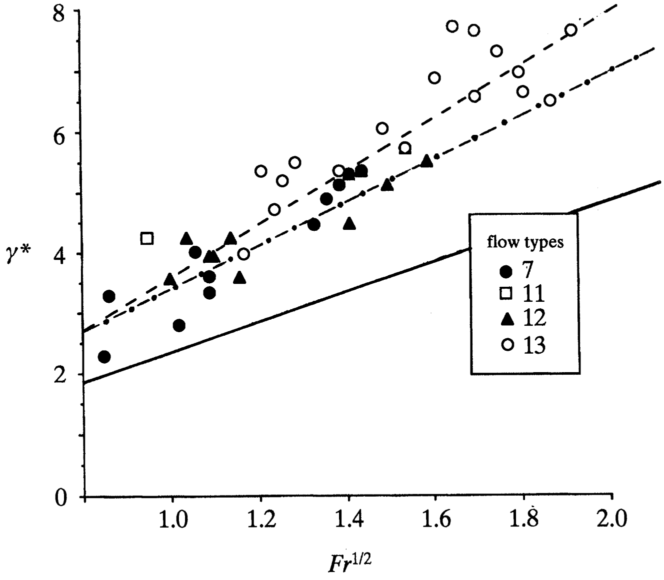

Figure 22. Composite plot of γ^* against $Fr^{1/2}$.Dotted line shows the result for steady flow (Boyer *et al.* 1989); chain line shows effect of redefining Fr in terms of $2u_0$; see text.

of Fr, the quantitative discrepancy between the steady and unsteady flow cases is reduced considerably, and the difference between the two estimator expressions (4.6) and (4.7) is seen to be within the scatter of the data.

The intra-cycle flow behaviour can be explored further, and the above conclusions confirmed, by plotting instantaneous intermediate values of $(\gamma^*)_{\rm i}$ against corresponding instantaneous values $(Fr_{\rm i}^{1/2})$ of $Fr^{1/2}$, within a given oscillation

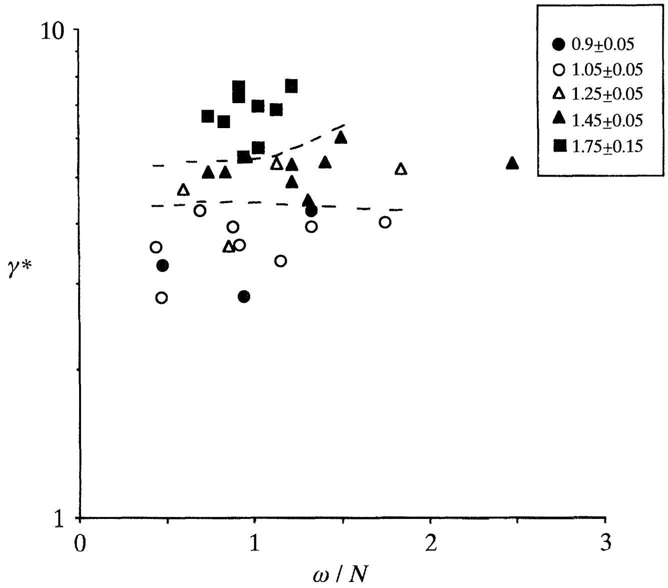

Figure 23. Plot of γ^* against Θ for Fr ranges indicated.

cycle. To accomplish this comparison, it was first of all necessary to determine the phase difference between the sinusoidal velocity field $u(t)$ of the forcing and the periodic pattern of the wake response $(\gamma^*)_\mathrm{i}(t)$ – see figure 20 – and then to correlate the two. Following equation (2.2), least squares fits were made to

$$\gamma = \gamma_0[1 - \alpha\cos(\omega t + \xi)] \tag{4.8}$$

for all of the γ data, where the amplitude α and the phase difference ξ were determined for each of the data-sets. Then, within the limits of validity of the model developed earlier in § 4 *b*(*ii*), it is then possible to relate (see (4.8)) each measured instantaneous value of $\gamma(t)$ to a corresponding instantaneous velocity $u_\mathrm{i}(t)$ and associated Froude number Fr_i given by

$$Fr_\mathrm{i} = Fr[1 - \cos(\omega t + \xi)]. \tag{4.9}$$

Because of the cosine form of $u(t)$, and the restriction in the experiments to a single value of unity for the velocity ratio Φ, the values of $Fr(t)$ and $Re(t)$ vary between 0 and $[2u_0/Nd]$ and 0 and $[2u_0d/v]$ respectively within a cycle. Thus, between these two sets of limiting values, only certain combinations of the instantaneous values Fr_i and Re_i correspond to flows in which the wakes are turbulent according to Boyer *et al.* (1989 *a*). In order to identify the subset of the complete $(\gamma^*)_\mathrm{i}$: $(Fr_\mathrm{i})^{1/2}$ data corresponding to turbulent wake structures, reference was made to the Fr : Re régime diagram constructed by Boyer *et al.* (1989 *a*) for steady counterpart flows. The bounding values of Fr and Re for the wake flow régimes delineated therein as turbulent, were then used to select the counterpart subset of turbulent wake data from the unsteady flow cases. Of course, implicit in such a procedure is the tacit assumption that the flow changes which take place within a cycle in the unsteady forcing experiments can be regarded as taking place sequentially in a number of transitions between quasi-steady states, each of which is characterized by the flow type determined by Boyer

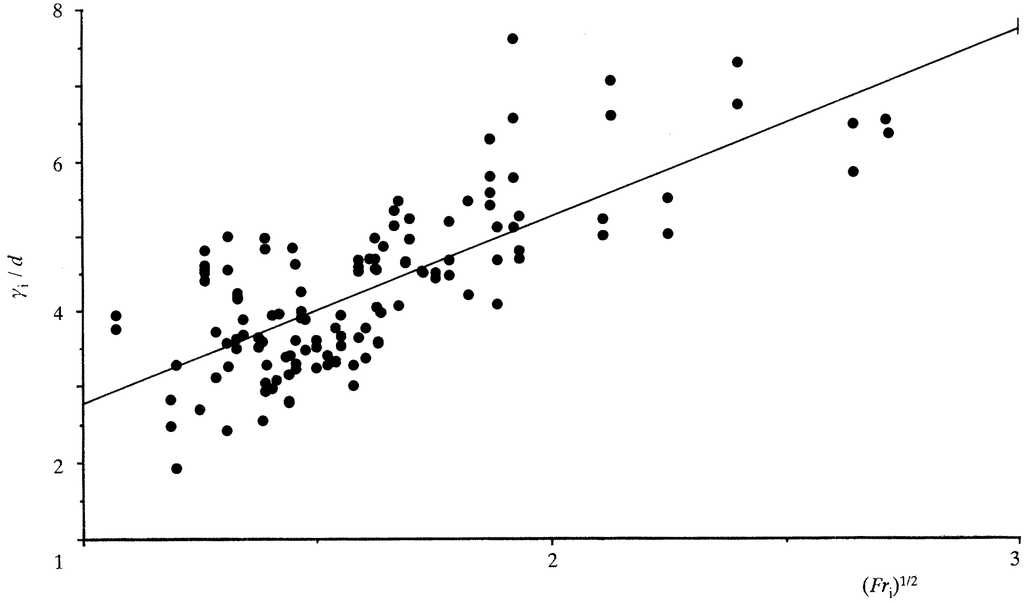

Figure 24. Plot of instantaneous values of dimensionless wake width γ_i/d against instantaneous Froude number $(Fr_i)^{1/2}$.

et al. (1989 *a*) for the instantaneous values of Fr and Re. As shown earlier in § 4 *b* and figure 20 *b*, this assumption will generally be valid for Type 7, 12 and 13 flows (the types under consideration here), and the above procedure thereby provides a self-consistent selection criterion for the composition of the $(\gamma_*)_i : Fr_i^{1/2}$ data subset corresponding to turbulent wake conditions. Figure 24 shows the resulting plot of the instantaneous turbulent wake widths $(\gamma^*)_i = {}_i/d$ versus $(Fr_i)^{1/2}$, for all of the turbulent wake flow Types (7, 12, and 13) shown earlier in figure 22. In spite of the scatter on the plot, and the number of simplifying assumptions underlying it, a linear regression fit reveals that the data are represented satisfactorily by a linear relationship,

$$(\gamma^*)_i = 2.44(Fr_i)^{1/2} + 0.40, \tag{4.10}$$

with a coefficient of determination of 0.55. This result, obtained from instantaneous turbulent wakes, is quantitatively consistent with not only the special maximum width case (see (4.6)) but also the earlier results of Boyer *et al.* (1989 *a*) for steady forcing.

5. Summary and concluding remarks

The experimental results presented above have demonstrated the richness and diversity of the flows associated with periodicity in the motion of a two-dimensional solid body through a stably stratified fluid. Attention has been directed particularly at delineating the flow features which characterize the effects of varying the frequency of the forced motion, over a wide range of both Froude and Reynolds numbers. The three-dimensional régime diagram shown in figure 14 summarizes the results of this effort, and the flow sequences of figures 2–13 show in detail the time-development of the individual flow types. For the portions of parameter space investigated in the experiments, the disturbances generated by the body were of relatively large amplitude, and comparisons of the observed lee wave characteristics with the predictions of linear theory were, of necessity, qualitative in nature and limited to the far-field. In spite of these restrictions, the limited data presented on this aspect of the flow show good qualitative agreement with theory.

The interplay between the different timescales (namely, N^{-1}, the buoyancy period, ω^{-1}, the forcing period, and u_0/d and u_1/d, the advective times) of the problem has been shown to affect in a crucial way the form of the downstream flow in the near-, intermediate- and far-wake regions. An important question in this connection has been the extent to which unsteady forcing of the flow can be regarded as proceeding step-wise in a series of quasi-steady stages, with consequent generation of instantaneous flow structures corresponding to steady flow patterns appropriate for the equivalent instantaneous values of the Froude and Reynolds numbers. Conversely, the issue to be addressed is that of determining the conditions under which flow structures associated solely with the unsteadiness of the motion are generated. Scalings based upon such considerations have been presented, and the associated prediction that the conditions $\Theta/Fr > 1$ and $Fr > 1$ should be satisfied simultaneously for the appearance of the features associated solely with unsteadiness, has been verified by the experimental data.

Scalings associated with the overshooting behaviour of the unsteady flow have also been developed, for viscous-dominated and inertia-dominated flows respectively, and these scalings been successful at not only classifying the degree of overshooting for different external flow parameters, but also quantifying the amount of forward overshooting of wake fluid for inertia-dominated flows. In cases for which the wake flows are turbulent, measurements have been made of the maximum vertical extent of the wake, as a function of (i) phase, (ii) Reynolds (Re) and Froude (Fr) number, and (iii) forcing frequency ratio, and these data have confirmed the sole dependence of this wake dimension upon $Fr^{1/2}$, in two respects; firstly, in the dependence of the maximum vertical extent over a full cycle upon the square root of the Froude number based upon the maximum velocity $2u_0$ within the cycle, and, secondly, in the dependence of the instantaneous maximum vertical extent of the wake at any time within the cycle upon $(Fr_{\mathrm{i}})^{1/2}$, with Fr defined in this case in terms of the corresponding instantaneous velocity at the time in question. In these respects, the wake dimensions for the unsteady forcing cases are controlled by the Froude number alone, in the manner of the steady flow counterpart situations investigated previously by Boyer *et al.* (1989*a*).

The authors are grateful for the financial support of the US Office of Naval Research, the US National Science Foundation, the UK Fellowship of Engineering and NATO Scientific Affairs Division. The invaluable technical expertise and assistance supplied by C. E. Porter, L. Montenegro, S. Ownbey, and G. Twitchell is also gratefully acknowledged, and Dr L. A. Mofor, Mr A. K. Munns and Ms F. Muir are thanked for their help with some of the processing of the experimental data. Dr T. N. Stevenson kindly supplied the plotting program for the internal wave phase configurations, and provided beneficial advice on their interpretation. He is thanked for this generosity.

References

Bannon, P. R. 1985 Flow acceleration and mountain drag. *J. Atmos. Sci.* **42**, 2445–2453.

Barti, C., Favier, D. P., Maresca, C. A. & Telionis, D. P. 1986 Vortex shedding and lock-on of a circular cylinder in oscillating flow. *J. Fluid Mech.* **170**, 527–544.

Bearman, P. W. & Graham, J. M. R. 1980 Vortex shedding from bluff bodies in oscillatory flow: a report on Euromech 119. *J. Fluid Mech.* **99**, 225–245.

Bearman, P. W., Graham, J. M. R., Naylor, P. & Obasaju, E. D. 1981 The role of vortices in oscillatory flow about bluff cylinders. In *Proc Int. Symp. Hydrodynamics in Ocean Engineering Trondheim, Norway*, pp. 621–643.

Bearman, P. W. & Obasaju, E. D. 1989 Transverse forces on a circular cylinder oscillating in-line with a steady current. In *Proc. 8th Int. Conf. on Offshore Mechanics and Arctic Engineering The Hague, Netherlands*, pp. 1–6.

Belotserkovskii, O. M., Belotserkovskii, S. O. & Pastushkov, A. R. 1987 Numerical modelling of internal waves in the flow of a stratified fluid over a semicircular obstacle. In *Problems in applied mathematics* (ed. O. M. Belotserkovskii), pp. 11–21. Moscow: Nauka. (In Russian.)

Boyer, D. L., Davies, P. A., Fernando, H. J. S. & Zhang, X. 1989*a* Linearly stratified flow past a horizontal circular cylinder. *Phil. Trans. R. Soc. Lond.* A**328**, 501–528.

Boyer, D. L., Zhang, X. & Davies, P. A. 1989 Time dependent rotating stratified flow past isolated topography. In *Mesoscale/synoptic coherent structures in geophysical turbulence* (ed. J. C. J. Nihoul & B. M. Jamart), pp. 655–670. Amsterdam: Elsevier.

Boyer, D. L. & Zhang, X. 1990 Motion of oscillatory currents past isolated topography. *J. Phys. Oceanogr.* **20**, 1425–1448.

Bukreev, V. I., Gusev, A. V. & Sturova, I. V. 1986 Generation of internal waves under the combined translational and vibrational motion of a cylinder in a fluid bilayer. *Zhurn. Prikladnoi Mekhaniki Tekhnicheskoi Fiz.* **3**, 63–70. (In Russian.)

Castro, I. P., Snyder, W. H. & Baines, P. G. 1990 Obstacle drag in stratified flow. *Proc. R. Soc. Lond.* A**429**, 119–140.

Davies, P. A., Boyer, D. L., Fernando, H. J. S. & Zhang, X. 1992 Wake flows in stratified fluids. In *Waves and turbulence in stratified flows* (ed. S. D. Mobbs & J. C. King), pp. 301–321. Oxford University Press.

Davies, P. A. 1992 Flow visualization and density field monitoring of stratified flows. *Optics Lasers Engng* **16**, 311–335.

Garrison, C. J. 1990 Drag and inertia forces on circular cylinders in harmonic flow. *J. Waterway Port. Coast. Ocean Engng ASCE* **116**, 169–190.

Griffin, O. M. & Ramberg, S. E. 1976 Vortex shedding from a cylinder vibrating in line with an incident normal flow. *J. Fluid Mech.* **75**, 257–271.

Hudspeth, R. T. 1991 Significance of the Keulegan–Carpenter parameter. *J. Hydraul. Engng ASCE* **117**, 1626–1638.

Kao, T. W., Pan, F.-S. & Renouard, D. 1985 Internal solitons on the pycnocline: generation, propogation and shoaling and breaking over a slope. *J. Fluid Mech.* **159**, 19–53.

Keulegan, G. H. & Carpenter, L. H. 1958 Forces on cylinders and plates in an oscillating fluid. *J. Res. natn. Bur. Stand.* **60**, 423–440.

Koop, C. G. & Butler, G. 1981 An investigation of internal solitary waves in a two-fluid system. *J. Fluid Mech.* **112**, 225–251.

Lighthill, M. J. 1967 On waves generated in dispersive systems by travelling forcing effects, with application to the dynamics of rotating fluids. *J. Fluid Mech.* **27**, 725–752.

Maxworthy, T. 1979 A note on internal solitary waves produced by tidal flow over a three dimensional ridge. *J. Geophys. Res.* **84**, 338–346.

Obasaju, E. D., Bearman, P. W. & Graham, J. M. R. 1988 A study of forces, circulation & vortex patterns around a circular cylinder in oscillating flow. *J. Fluid Mech.* **196**, 467–494.

Ongoren, A. & Rockwell, D. 1988*a* Flow structure from an oscillating cylinder. Part 1: Mechanisms of phase shift and recovery in the near wake. *J. Fluid Mech.* **191**, 197–223.

Ongoren, A. & Rockwell, D. 1988*b* Flow structure from an oscillating cylinder. Part 2: Mode competition in the near wake. *J. Fluid Mech.* **191**, 225–245.

Oster, G. 1965 Density gradients. *Scientific Am.* **213**, 70–76.

Stevenson, T. N. & Thomas, N. H. 1969 Two-dimensional internal waves generated by a travelling oscillating cylinder. *J. Fluid Mech.* **36**, 505–511.

Stevenson, T. N. 1973 The phase configuration of internal waves around a body moving in a density stratified fluid. *J. Fluid Mech.* **60**, 759–767.

Sumer, B. M. & Fredsøe, J. 1988 Transverse vibrations of an elastically mounted cylinder exposed to an oscillating flow. *J. Offshore Mech. Arctic Engng* **110**, 387–394.

Sumer, B. M. & Fredsøe, J. 1989*a* Effect of Reynolds number on vibrations of cylinders. *J. Offshore Mech. Arctic Engng* **111**, 131–137.

Sumer, B. M., Fredsøe, J., Graveson, H. & Bruschi, X. 1989*b* Response of marine pipelines in scour trenches. *J. Waterway Port. Coastal Ocean Engng* **115**, 477–496.

Sumer, B. M., Jensen, B. L. & Fredsøe, J. 1991 Effect of a plane boundary on oscillatory flow around a circular cylinder. *J. Fluid Mech.* **225**, 271–300.

Taneda, S. 1956 Experimental investigation of the wakes behind cylinders and plates at low Reynolds numbers. *J. Phys. Soc. Japan* **11**, 302–307.

Tanida, Y., Okajima, A. & Watanabe, Y. 1973 Stability of a circular cylinder oscillating in uniform flow or in a wake. *J. Fluid Mech.* **61**, 769–784.

Williamson, C. H. K. 1985 Sinusoidal flow relative to circular cylinders. *J. Fluid Mech.* **155**, 141–174.

Received 5 June 1992; accepted 12 March 1993

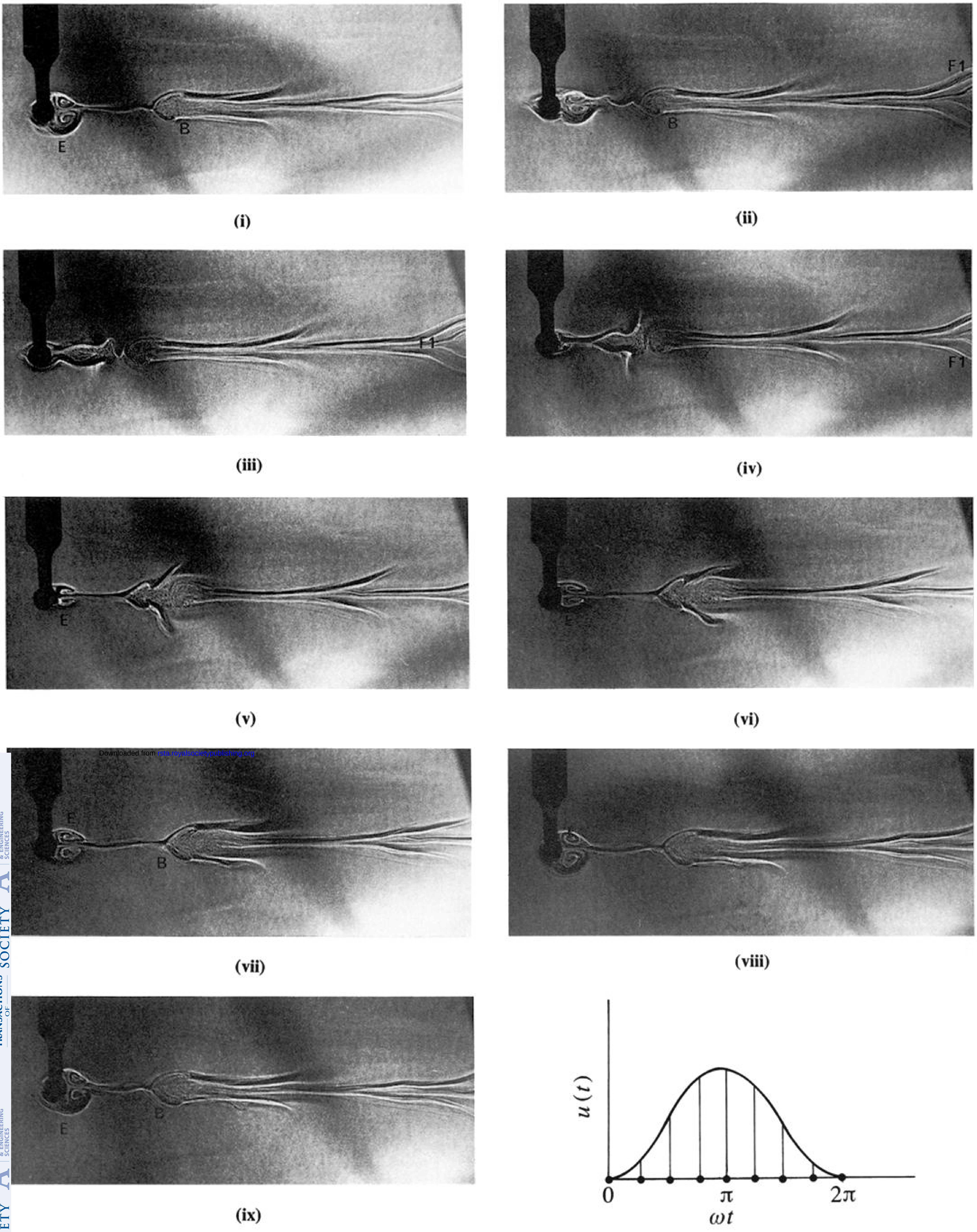

(i) (ii) (iii) (iv) (v) (vi) (vii) (viii) (ix)

Figure 2. Sequence of photographs taken at phases ωt: (i) $2n\pi$, (ii) $2n\pi + (\frac{1}{4}\pi)$, (iii) $2n\pi + (\frac{1}{2}\pi)$, (iv) $2n\pi + (\frac{3}{4}\pi)$, (v) $2n\pi + \pi$, (vi) $2n\pi + (\frac{5}{4}\pi)$, (vii) $2n\pi + (\frac{3}{2}\pi)$, (viii) $2n\pi + (\frac{7}{4}\pi)$, and (ix) $2\pi(n+1)$ within a single oscillation cycle, for $Re = 159$, $Fr = 0.61$, $\Theta = 0.58$, $\Phi = 1$, and $d/H = 0.11$. Type 2 flow.

Figure 3

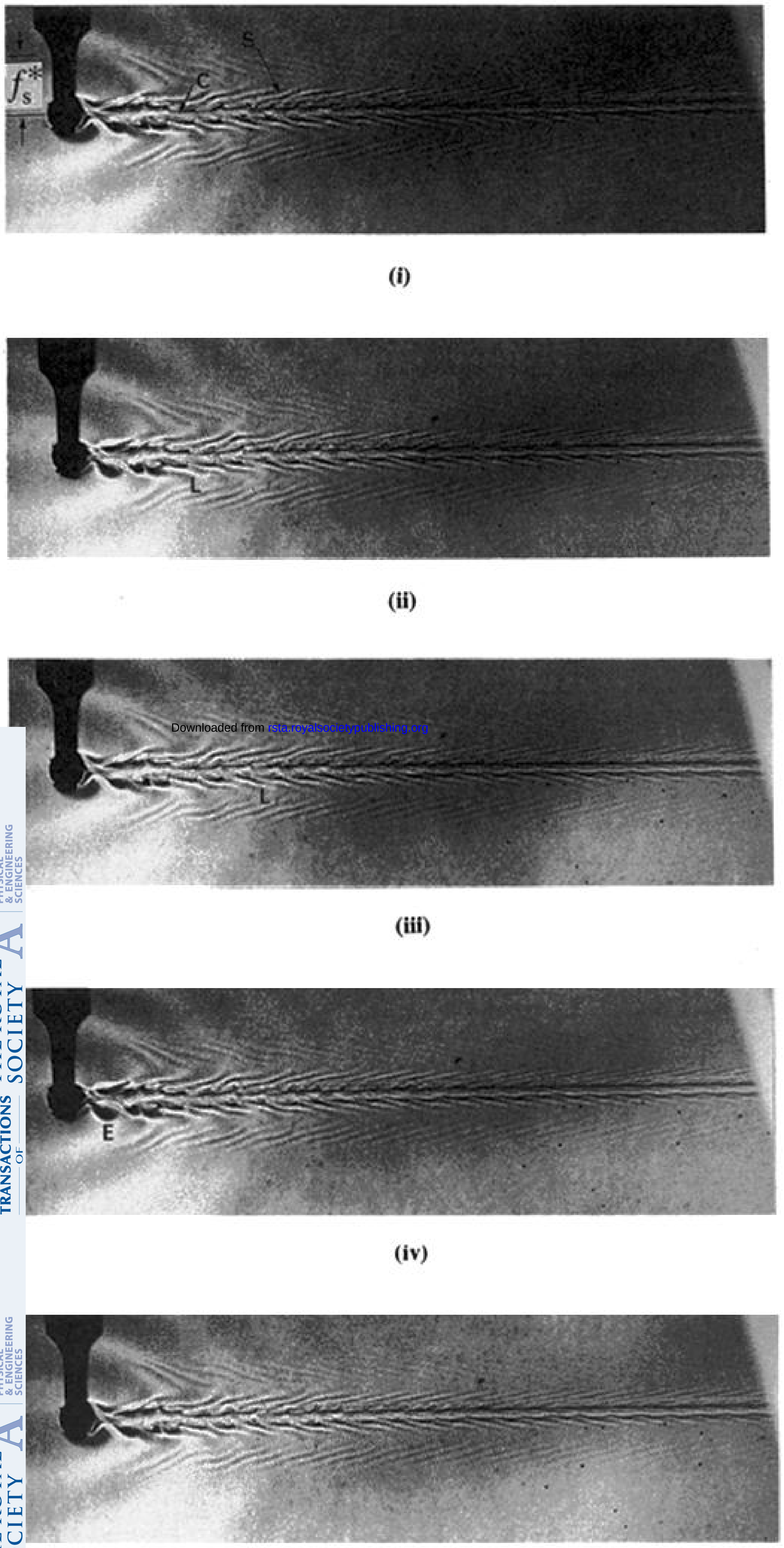

(i)

(ii)

(iii)

(iv)

(v)

Figure 4

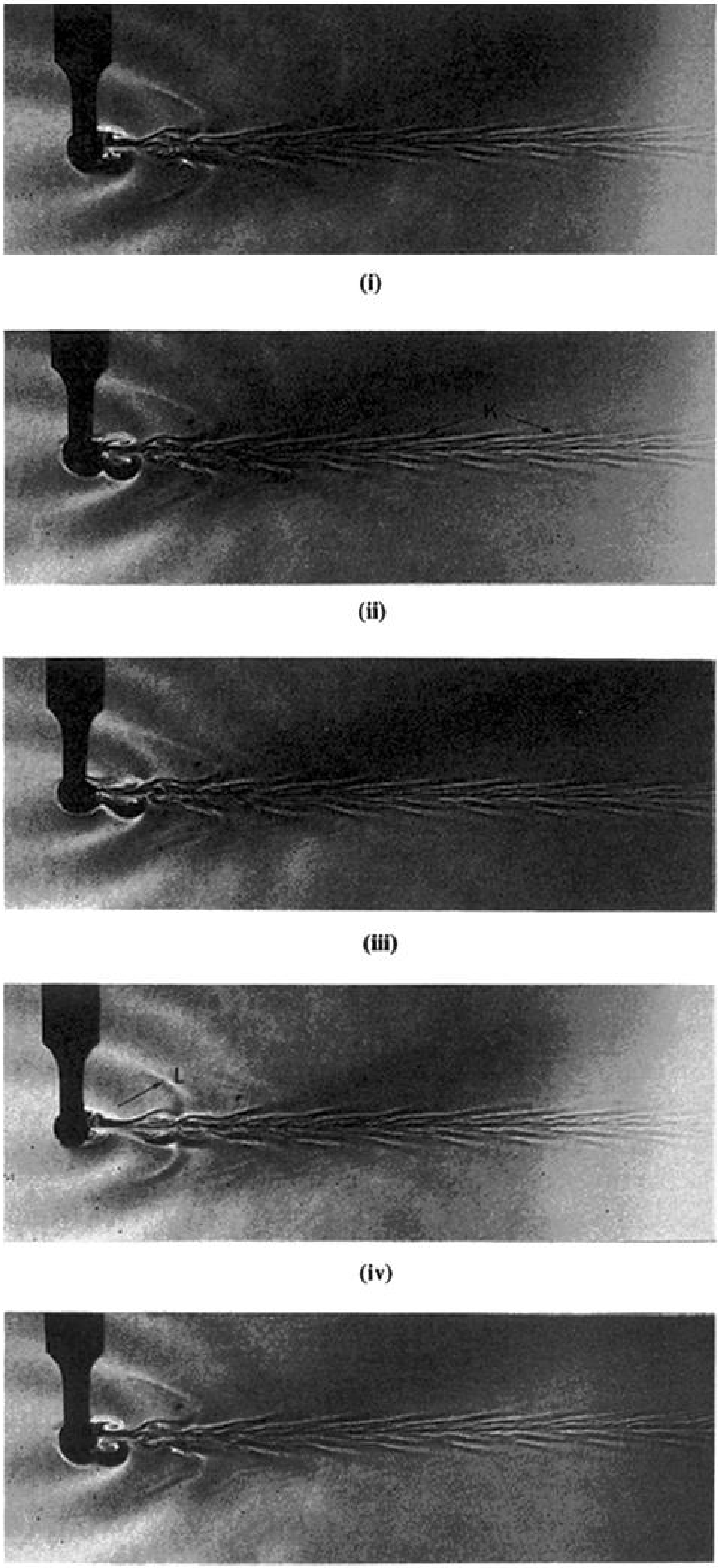

(i)

(ii)

(iii)

(iv)

(v)

igure 3. Type 3 flow, showing predicted separation f_s^* of steady waves (see equation (4.1)). ame legend as figure 2, except $Re = 79$, $Fr = 0.23$, and $\Theta = 1.79$.

igure 4. Type 4 flow. Same legend as figure 2, except $Re = 79$, $Fr = 0.24$, and $\Theta = 0.94$.

Figure 5

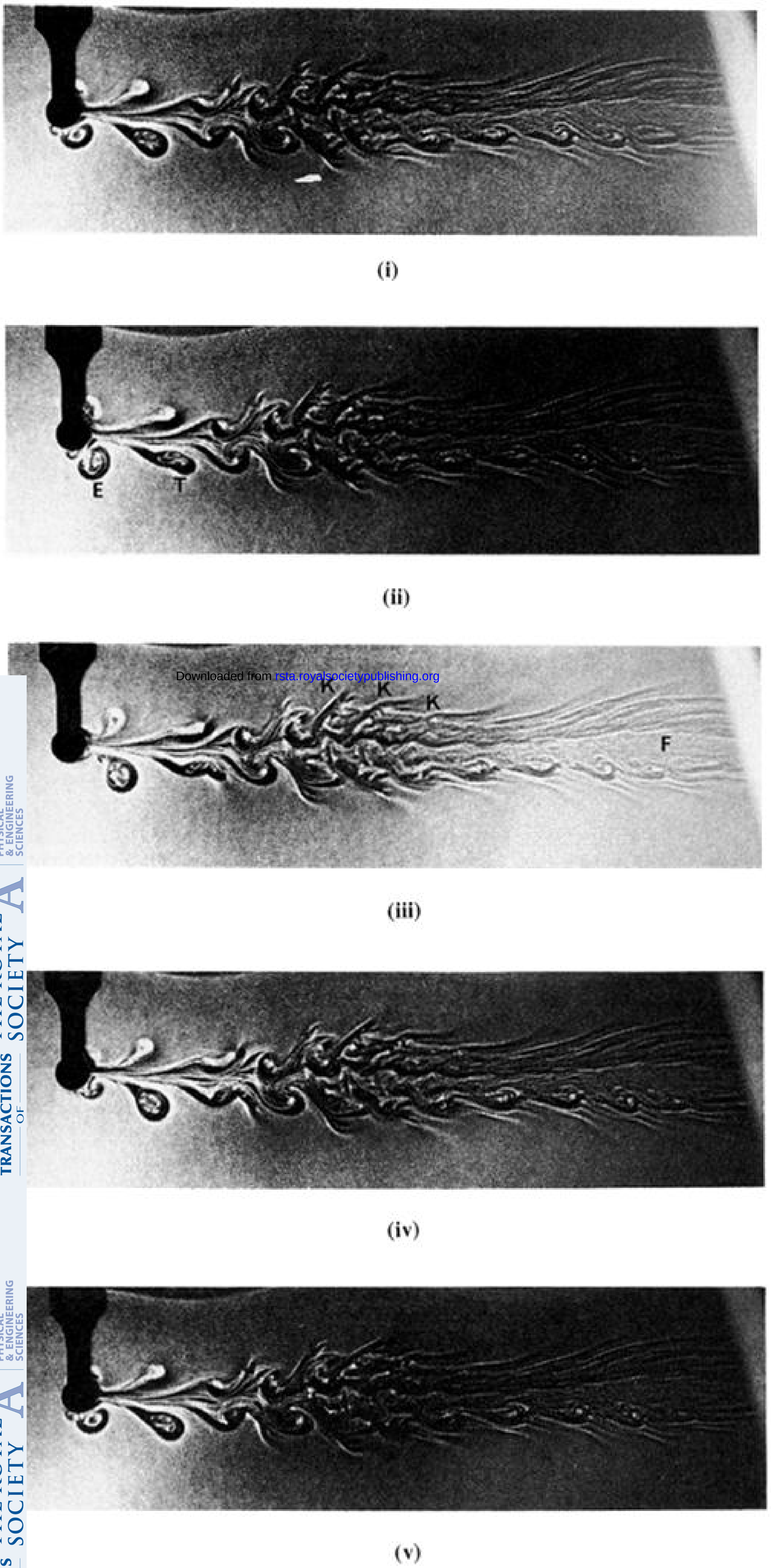

Figure 6

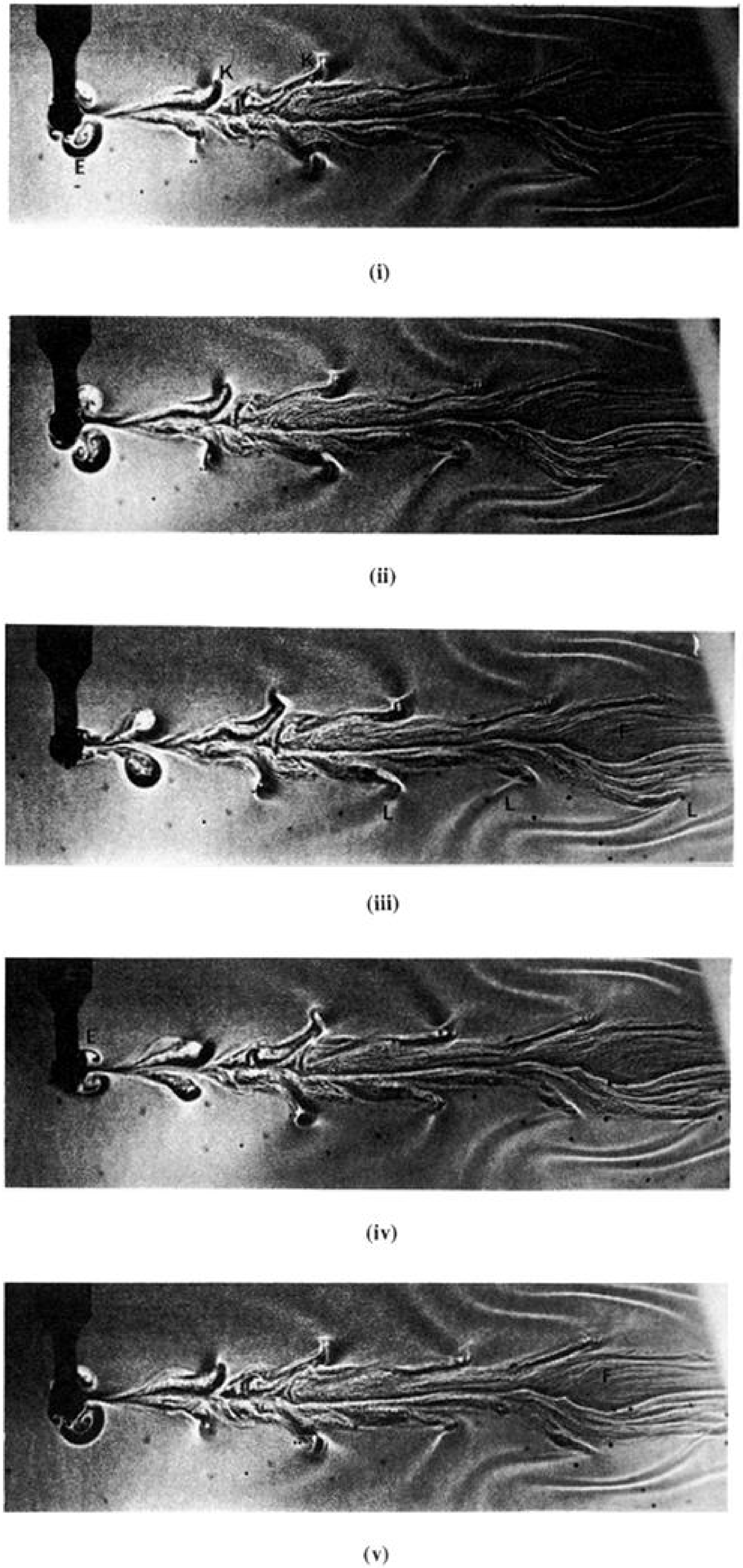

Figure 5. Type 5 flow. Same legend as figure 2, except $Re = 238$, $Fr = 0.96$, and $\Theta = 3.09$.

Figure 6. Type 6 flow. Same legend as figure 2, except $Re = 238$, $Fr = 0.69$, and $\Theta = 1.77$.

Figure 7

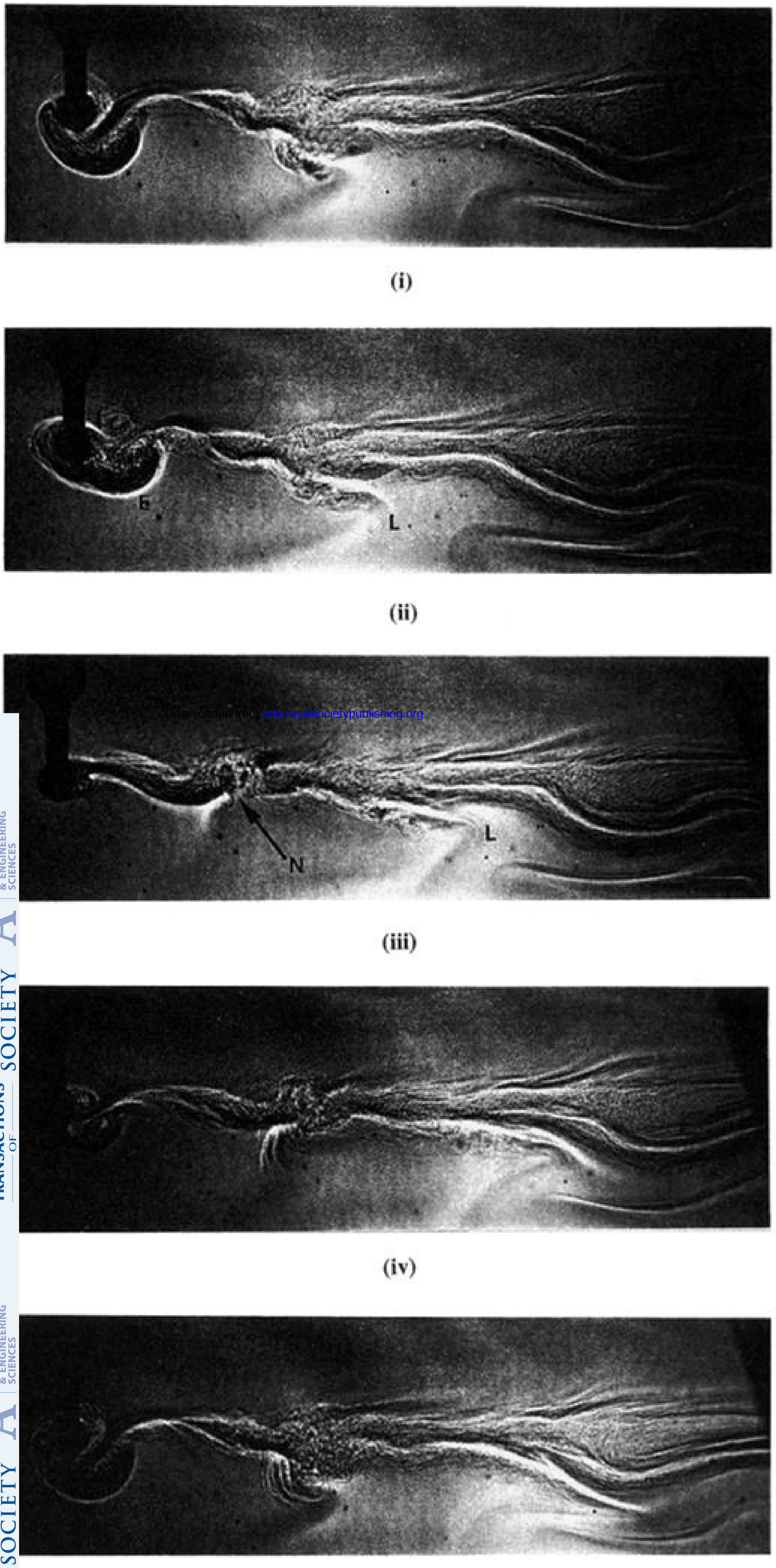

(i)

(ii)

(iii)

(iv)

(v)

Figure 8

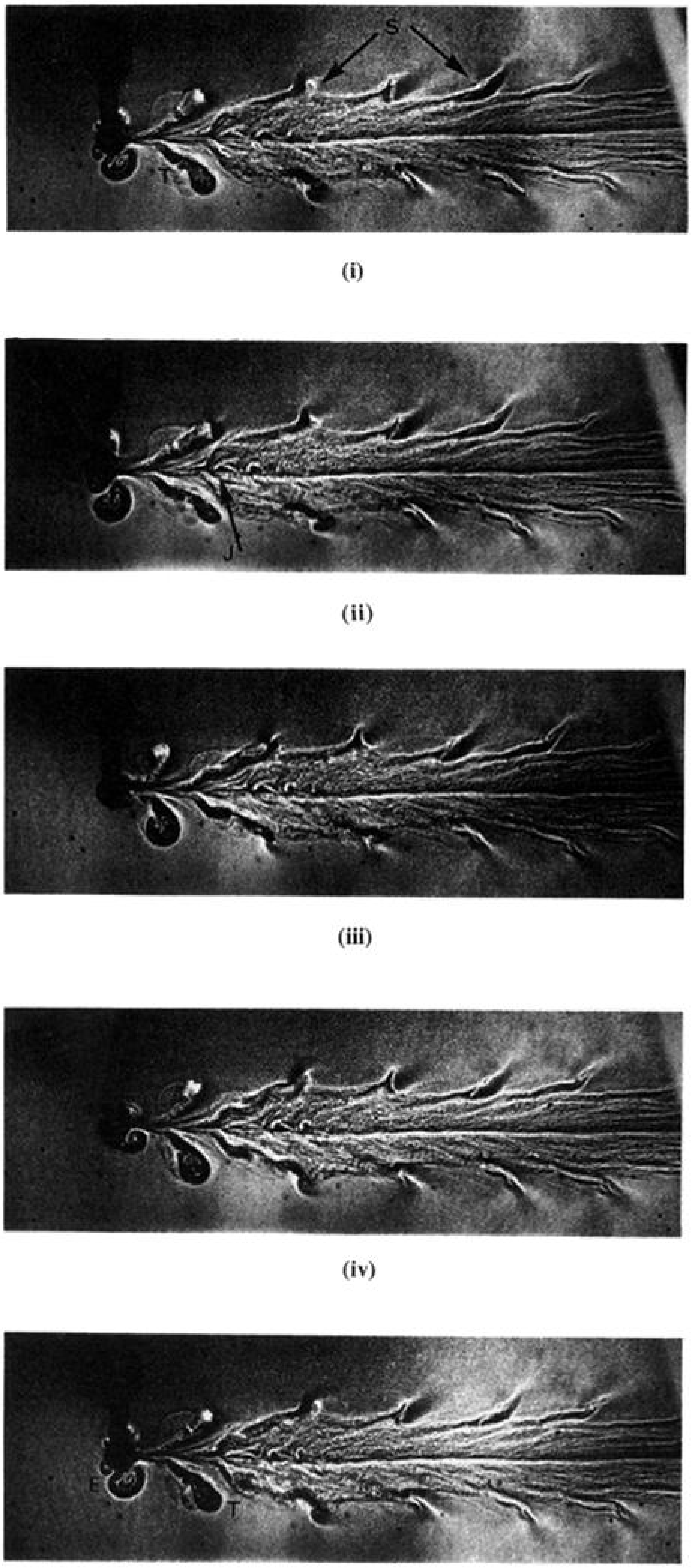

(i)

(ii)

(iii)

(iv)

(v)

igure 7. Type 7 flow. Same legend as figure 2, except $Re = 238$, $Fr = 0.73$, and $\Theta = 0.94$.

igure 8. Type 8 flow. Same legend as figure 2, except $Re = 318$, $Fr = 0.93$, and $\Theta = 2.66$.

Figure 9

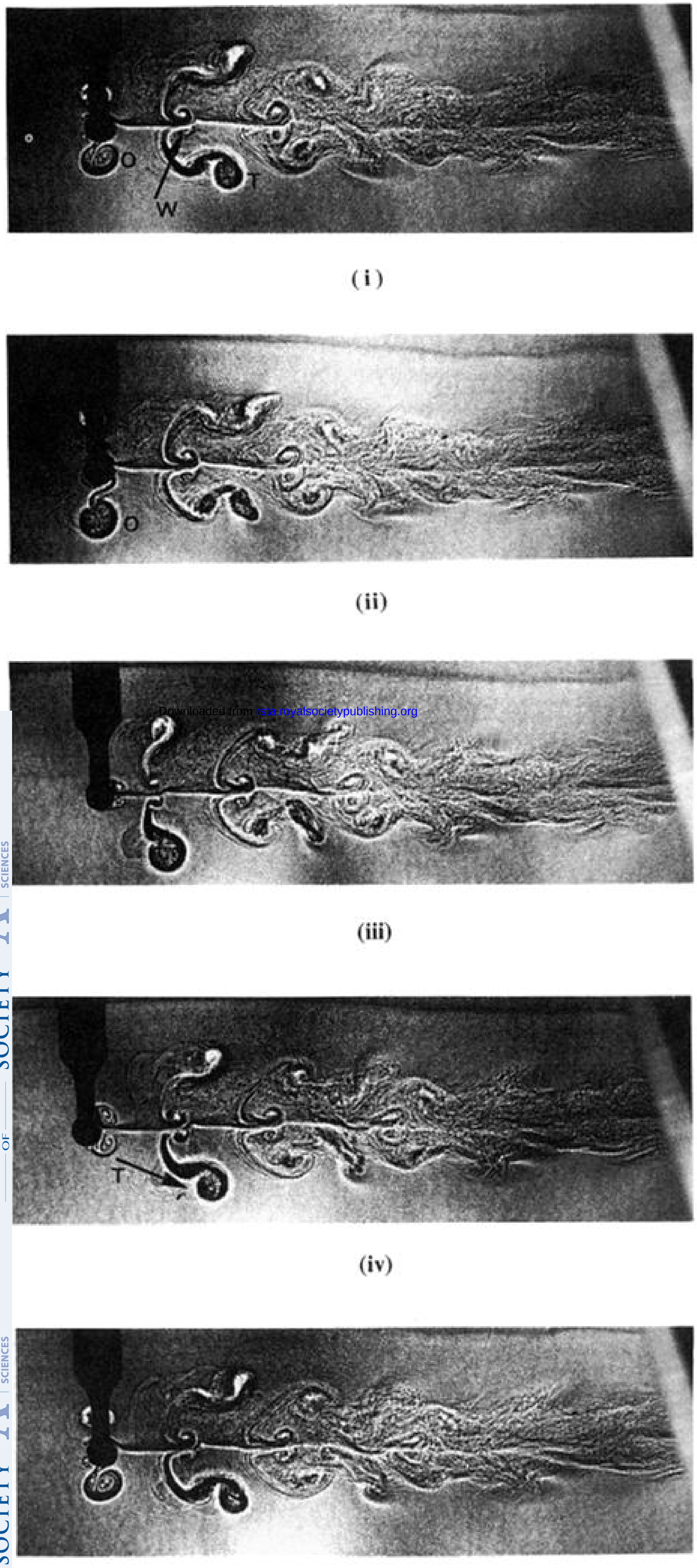

(i)

(ii)

(iii)

(iv)

(v)

Figure 10

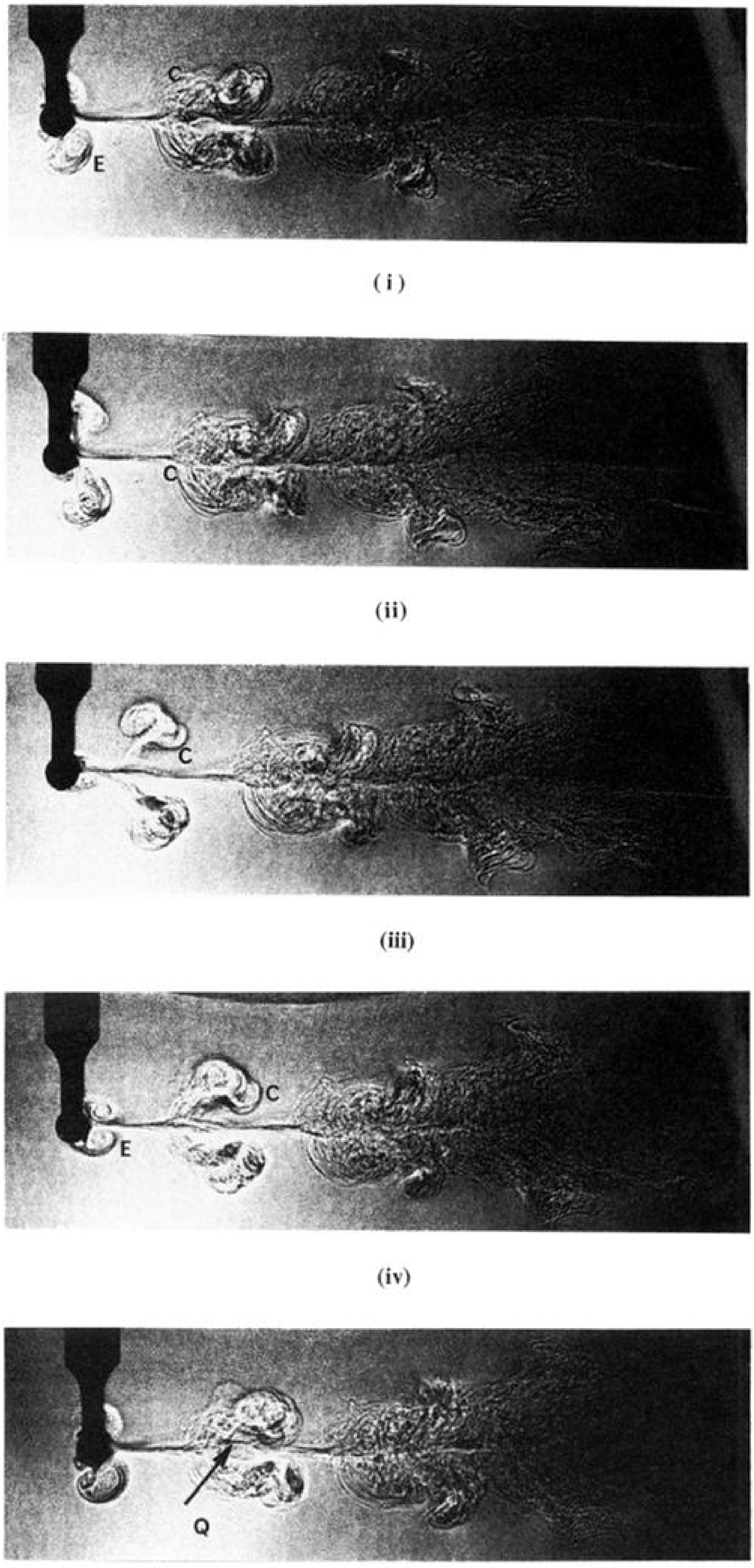

(i)

(ii)

(iii)

(iv)

(v)

Figure 9. Type 9 flow. Same legend as figure 2, except $Re = 397$, $Fr = 1.59$, and $\Theta = 2.45$.

igure 10. Type 10 flow. Same legend as figure 2, except $Re = 318$, $Fr = 1.37$, and $\Theta = 2.64$.

Figure 11

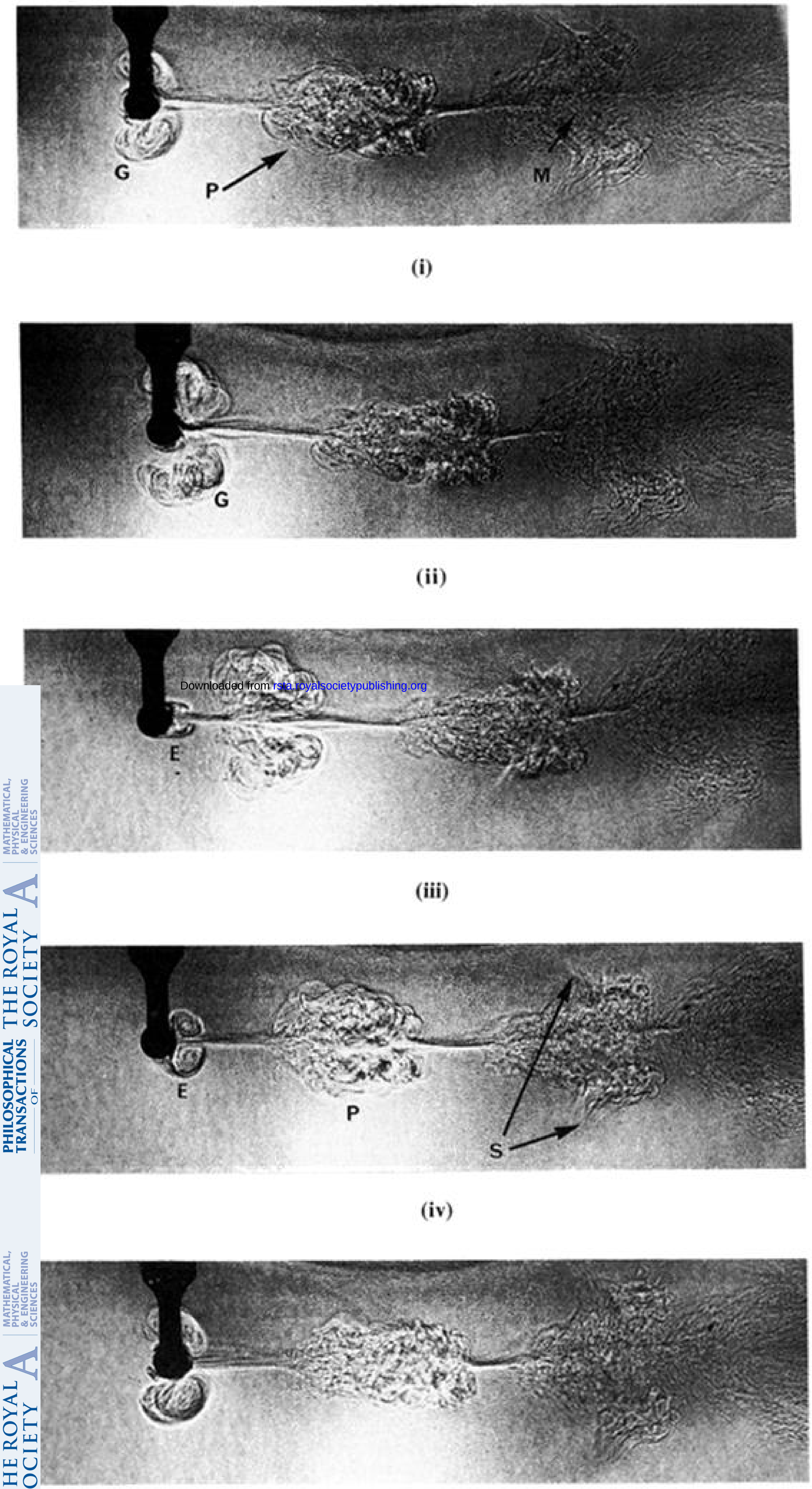

(i)

(ii)

(iii)

(iv)

(v)

Figure 12

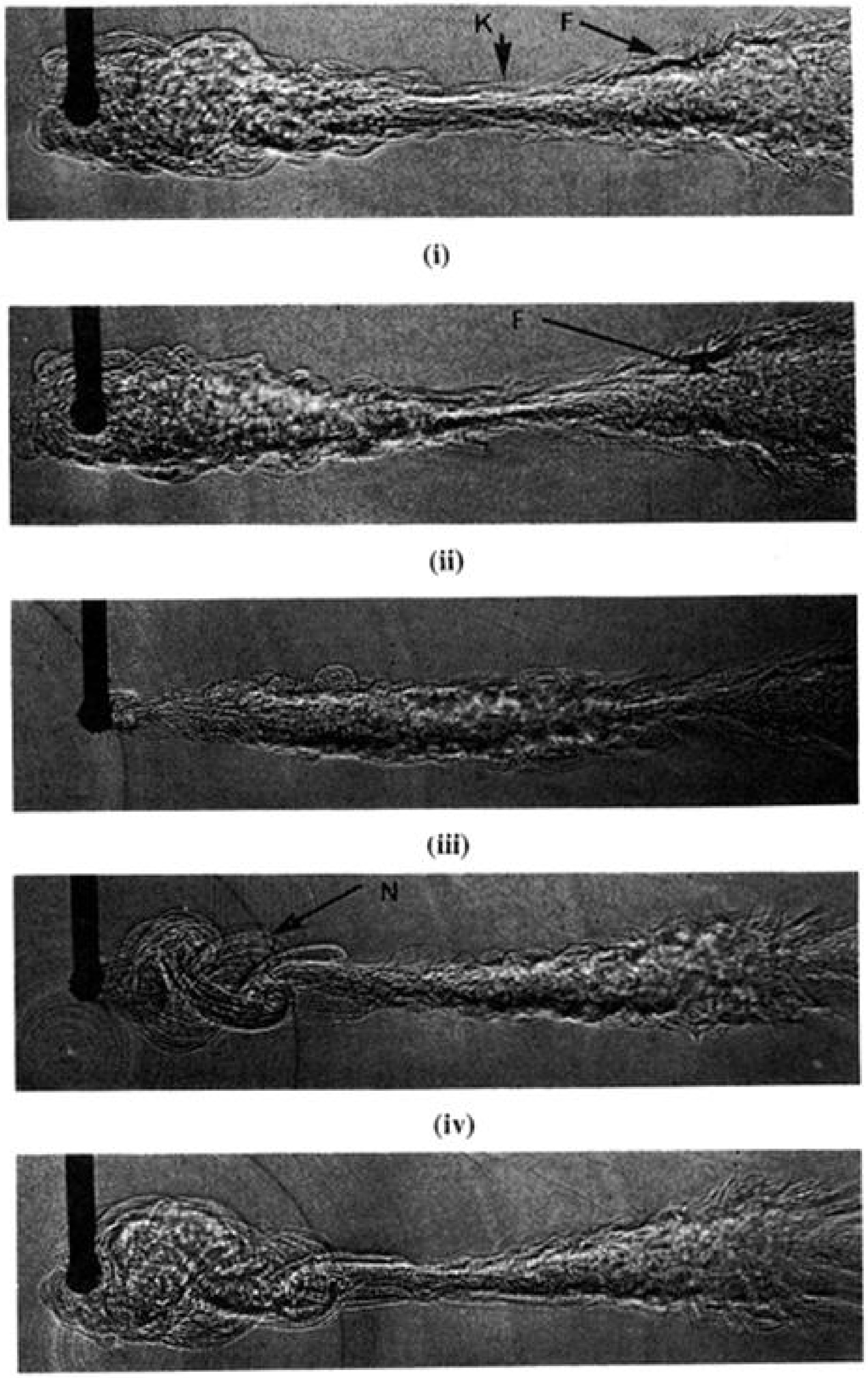

(i)

(ii)

(iii)

(iv)

(v)

igure 11. Type 11 flow. Same legend as figure 2, except $Re = 318$, $Fr = 1.31$, and $\Theta = 1.90$.

igure 12. Type 12 flow. Same legend as figure 2, except $Re = 381$, $Fr = 2.52$, and $\Theta = 0.94$.

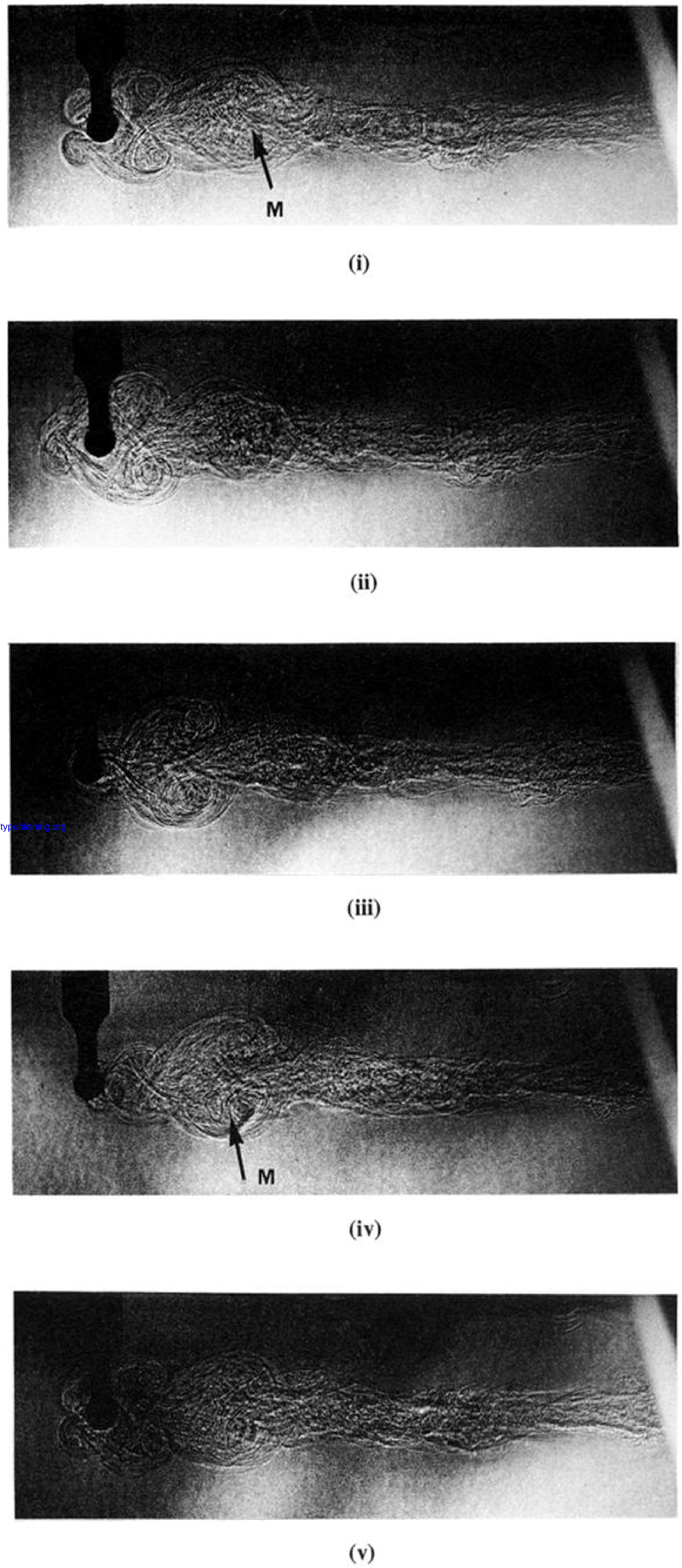

(i)

(ii)

(iii)

(iv)

(v)

igure 13. Type 13 flow. Same legend as figure 2, except $Re = 397$, $Fr = 1.59$, and $\Theta = 1.84$.

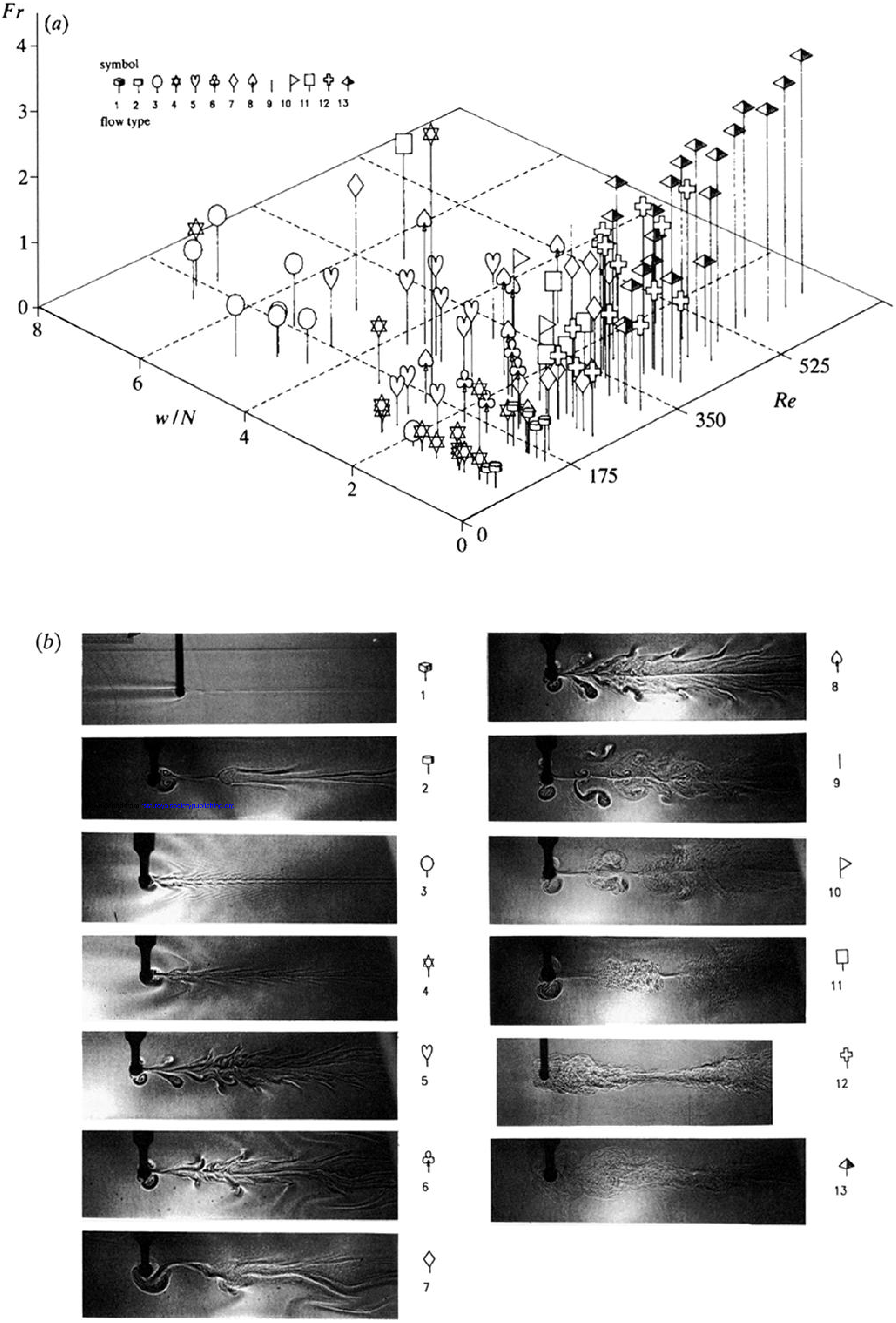

Figure 14. Three-dimensional $(Fr : \omega/N : Re)$ régime diagram showing the occurrence of the flow Types 1–13 described in § 4 *b*. See attached key for identification and illustration of flow types.